Quiescence Modulates Stem Cell Maintenance and Regenerative Capacity in the Aging Brain

Graphical Abstract

Highlights

- Time-dependent stem cell depletion levels off in the old brain via increased quiescence

- Age minimally changes the neural stem cell transcriptome

- Once-activated neural stem cells perform similar in the old and young brain

- The old niche keeps stem cells quiescent via inflammation and Wnt activity regulation

Authors

Georgios Kalamakis, Daniel Brüne, Srikanth Ravichandran, ..., Antonio del Sol, Anna Marciniak-Czochra, Ana Martin-Villalba

Correspondence

a.martin-villalba@dkfz-heidelberg.de

In Brief

Aged brains have a small number of highly quiescent neural stem cells that, upon activation, functionally resemble young stem cells; it is the niche itself that becomes more inflammatory and drives this quiescence.
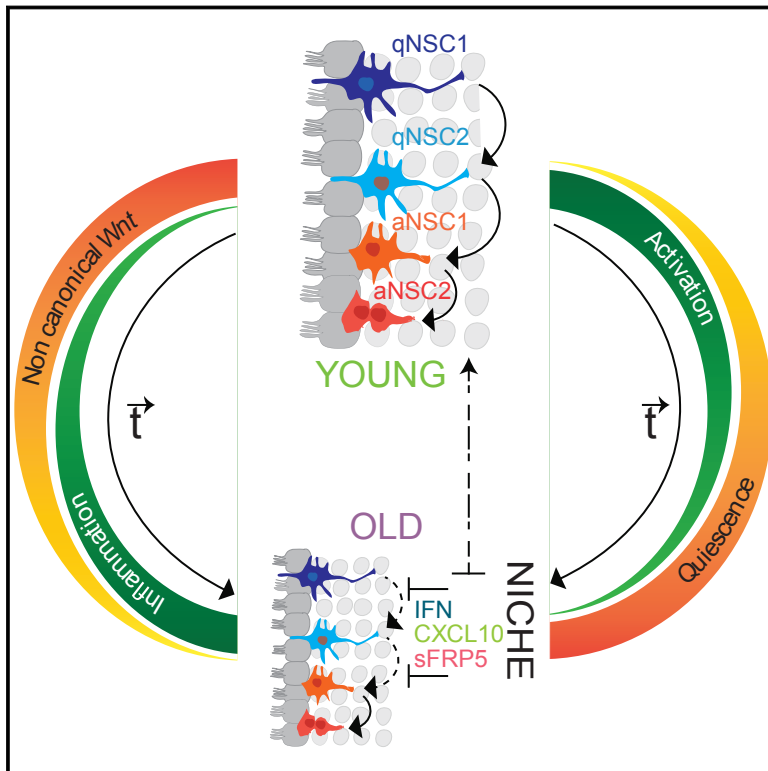
Article

Quiescence Modulates Stem Cell Maintenance and Regenerative Capacity in the Aging Brain

Georgios Kalamakis,[1,2] Daniel Brüne,[1] Srikanth Ravichandran,[3] Jan Bolz,[1] Wenqiang Fan,[7,8] Frederik Ziebell,[1,11]
Thomas Stiehl,[11] Francisco Catalá-Martinez,[1] Janina Kupke,[1] Sheng Zhao,[1] Enric Llorens-Bobadilla,[1] Katharina Bauer,[12]
Stefanie Limpert,[1] Birgit Berger,[1] Urs Christen,[13] Peter Schmezer,[14] Jan Philipp Mallm,[15,16] Benedikt Berninger,[7,8,9,10]
Simon Anders,[17,18] Antonio del Sol,[3,4,5,6,18] Anna Marciniak-Czochra,[11,18] and Ana Martin-Villalba[1,19,*]
[1]Molecular Neurobiology, German Cancer Research Center, 69120 Heidelberg, Germany
[2]University of Heidelberg, 69120 Heidelberg, Germany
[3]Luxembourg Centre for Systems Biomedicine, University of Luxembourg, 4362, Luxembourg
[4]CIC bioGUNE, 48160 Derio, Spain
[5]IKERBASQUE, Basque Foundation for Science, 48009 Bilbao, Spain
[6]Moscow Institute of Physics and Technology, 141700 Dolgoprudny, Russia
[7]Institute of Physiological Chemistry, University Medical Center Johannes Gutenberg University Mainz, 55128 Mainz, Germany
[8]Focus Program Translational Neuroscience, Johannes Gutenberg University Mainz, 55131 Mainz, Germany
[9]Institute of Psychiatry, Psychology & Neuroscience, Centre for Developmental Neurobiology, King's College London, London SE1 1UL, UK
[10]Institute of Psychiatry, Psychology & Neuroscience, MRC Centre for Neurodevelopmental Disorders, King's College London,
London SE1 1UL, UK
[11]Institute of Applied Mathematics, Interdisciplinary Center for Scientific Computing and Bioquant, Heidelberg University, 69120 Heidelberg,
Germany
[12]Heidelberg Center for Personalized Oncology (DKFZ-HIPO), German Cancer Research Center, 69120 Heidelberg, Germany
[13]Goethe University Hospital Frankfurt/ZAFES, 60596 Frankfurt, Germany
[14]German Cancer Research Center, Division of Epigenomics and Cancer Risk Factors, 69120 Heidelberg, Germany
[15]Division Chromatin Networks, German Cancer Research Center, 69120 Heidelberg, Germany
[16]Single-cell Open Lab, German Cancer Research Center, 69120 Heidelberg, Germany
[17]Center for Molecular Biology, Heidelberg University, 69120 Heidelberg, Germany
[18]These authors contributed equally
[19]Lead Contact
*Correspondence: a.martin-villalba@dkfz-heidelberg.de
https://doi.org/10.1016/j.cell.2019.01.040

SUMMARY

The function of somatic stem cells declines with age. Understanding the molecular underpinnings of this decline is key to counteract age-related disease. Here, we report a dramatic drop in the neural stem cells (NSCs) number in the aging murine brain. We find that this smaller stem cell reservoir is protected from full depletion by an increase in quiescence that makes old NSCs more resistant to regenerate the injured brain. Once activated, however, young and old NSCs show similar proliferation and differentiation capacity. Single-cell transcriptomics of NSCs indicate that aging changes NSCs minimally. In the aging brain, niche-derived inflammatory signals and the Wnt antagonist sFRP5 induce quiescence. Indeed, intervention to neutralize them increases activation of old NSCs during homeostasis and following injury. Our study identifies quiescence as a key feature of old NSCs imposed by the niche and uncovers ways to activate NSCs to repair the aging brain.

INTRODUCTION

In the adult murine brain, neural stem cells (NSCs) residing within the ventricular-subventricular zone (V-SVZ) of the lateral ventricles generate olfactory bulb (OB) interneurons required to fine-tune odor discrimination throughout the life of the animal. Recent studies have characterized the division mode and the transcriptional programs underlying the different activation states of NSCs in the young brain. Yet, whether this default program is affected by age and how this potentially influences NSC function is controversial. In the old brain, NSCs retain the ability to generate the different subtypes of OB interneurons, albeit at much lower numbers (Basak et al., 2018; Dulken et al., 2017; Llorens-Bobadilla et al., 2015; Obernier et al., 2018; Shook et al., 2012). Whereas some studies report a decreased proliferation of NSCs (Capilla-Gonzalez et al., 2014; Shi et al., 2018; Silva-Vargas et al., 2016), others report no changes or even an increase in proliferation (Ahlenius et al., 2009; Shook et al., 2012). In the human brain, generation of new neurons is debated (Kempermann et al., 2018). In the adult human brain, C14 birth dating studies have revealed the existence of new neurons in the striatum, and the V-SVZ NSCs are regarded as the source of these striatal interneurons (Ernst et al., 2014).

The present study addresses the stem cell dynamics within the V-SVZ throughout the life of the animal. Mathematical modeling

Cell

is used to explore how time-dependent changes in key stem cell features can explain the age-dependent decline of the NSC pool. Profiling of the single transcriptomes of young and aged NSCs and of the transcriptomes of neighboring niche cells is used to identify drivers of this age-dependent change. Altogether, this study advances our understanding of the molecular underpinnings of age-related decline in NSC function.

RESULTS

A Time-Dependent Increase in Quiescence Maintains a Stem Cell Reservoir at Old Age while Making Stem Cells More Resistant to Activation

To assess age-related changes of NSCs, we quantified the numbers of NSCs and their immediate progeny across different ages. To this end, we performed fluorescence-activated cell sorting (FACS) analysis of different cell subpopulations isolated from the V-SVZ of 2-, 7-, and 22-month-old (MO) mice (Figures 1A and S6A). This analysis revealed that the total number of NSCs significantly declines between 2 and 7 MO and remains low at 22 MO. We further analyzed the numbers of quiescent NSCs (qNSCs), active NSCs (aNSCs), and transit amplifying progenitors (TAPs). All three populations showed similar dynamics, with a significant decrease from 2 to 7 MO, and low numbers from 7 to 22 MO. To confirm this observation, we quantified NSCs and their progeny within the V-SVZ *in situ*. The TLX-CreER^{T2}YFP reporter mouse line was used to label NSCs (Liu et al., 2008). To additionally identify progenitors that became quiescent at embryonic day 14 (E14) and only got reactivated in the adult V-SVZ (Fuentealba et al., 2015), we administered bromodeoxyuridine (BrdU) at E14. Note that every labeling protocol used in this study can be found in Figure S5A. The number of embryonic label-retaining NSCs (E-LRCs) drastically decreased between 2 and 14 MO (Figures 1B and 1C). Together, these data show a rapid decline of the number of NSCs from 2 to 7 MO that slows down thereafter.

Others have reported this age-dependent decrease of NSC number; however, the NSC features that have to change with time to explain this decline have not been addressed. To this end, we built a mathematical model (MM) of V-SVZ NSC dynamics (Data S1), based on a mathematical framework developed to describe adult hippocampal neurogenesis (Ziebell et al., 2014, 2018). For model fitting, we considered a joint dataset consisting of the subset of the frequency of active cells as a fraction of the adult label-retaining cells (LRCs) (14 days BrdU administration in drinking water followed by 14 days of chase time before sacrificing the animals at indicated ages; Figure S5) and of the subset of active cells as a fraction of the TLX-labeled cells (Figures S1A–S1D and S5). We fit the model using both subsets simultaneously. Based on our own experimental data and current literature (Basak et al., 2018; Obernier et al., 2018), we assumed that qNSCs can enter cell cycle to become aNSCs and give rise to either two qNSCs or two TAPs with the capacity of performing *n* symmetric self-renewing divisions (Figure 1D). This is different from the assumptions we used in our previous work on NSC dynamics in the hippocampus, where we allowed additional NSC fates like asymmetric divisions or depletion through cell death or direct transformation into astrocytes (Ziebell et al., 2014, 2018).

First, we designed a model with cell parameters that do not change in time and evaluated its outcome by comparing it to experimental data. The assumption of time-constant parameters, called "no-aging" scenario, led to an exponential decay of the total NSC number, which did not match the experimental observation of saturation of the decline of NSC numbers at an older age (Figure 1E, left). Furthermore, contrary to the experimental data, the model with this assumption predicted that the fraction of active among all LRCs and TLX-labeled cells would not change over time (Figure 1E, right). To identify mechanisms that might explain the observed decline in the fraction of the active cells, we considered three age-dependent scenarios: increase in cell-cycle length, increase in self-renewal, and increase of the mean time spent in quiescence (Figures 1F–1H; Data S1). To compare model predictions to experimental data, we examined the following time-dependent quantities: number of NSCs and the fraction of active cells among adult LRCs and TLX-labeled cells.

We first assumed, as previously suggested by Daynac et al. (2016), that upon aging, aNSCs require progressively more time to complete their cell cycle (without taking into account time in G0 phase). As in the no-aging scenario, this led to dynamics with faster depletion of the total number of NSCs (Figure 1F, left) and time-constant fraction of aNSCs (Figure 1F, right). In the second scenario, we modeled an age-related increase of the fraction of self-renewal, i.e., assuming that upon aging a higher fraction of aNSCs divisions results in two qNSCs rather than two TAPs. This model correctly reproduced the saturation in the decay of the total number of NSCs (Figure 1G, left) but showed only a 3.5% decline in the fraction of aNSCs in contrast to the 37% decline observed in the experimental data and it would require a low fraction of aNSCs in young mice (Figure 1G, right). In addition, the model predicted a rapid decline in the number of NSCs at young age, which would require a much larger number of cells (1.1×10^{6} cells) at the beginning of the process (Figure S1E). Finally, we assumed that the time NSCs spend in quiescence (G0) increases with age. Changes in this feature fit the experimental data best, because they are not only showing the saturation of the decline in total NSC numbers (Figure 1H, left) but also the drop in the fraction of aNSCs (35% in the model simulation versus 37% in the data) (Figure 1H, right). The conclusion that only the increasing quiescence scenario can explain the data is supported by the Akaike information criterion (AIC) (Tables S1, S2, and S3; Data S1). To further validate our results, we considered a model with two time-dependent cell parameters accounting for both simultaneous increase of the fraction of NSC self-renewal and increase of the mean time spent by a cell in quiescence. Although increasing the number of free parameters allows finding a fit that seems closer to the data, the model combining two time-dependent parameters was not superior in terms of AIC. To quantify the contribution of changes of both factors to the optimal fit, we extracted the dynamics of the two parameters from the model (Figure S1F; Tables S1, S2, and S3; Data S1). Comparison of the estimated cell properties in the different models showed that even if the two parameters undergo age-dependent changes, the major component of the regulatory process that explains the observed dynamics is the increase in time spent in quiescence (decreasing rate of
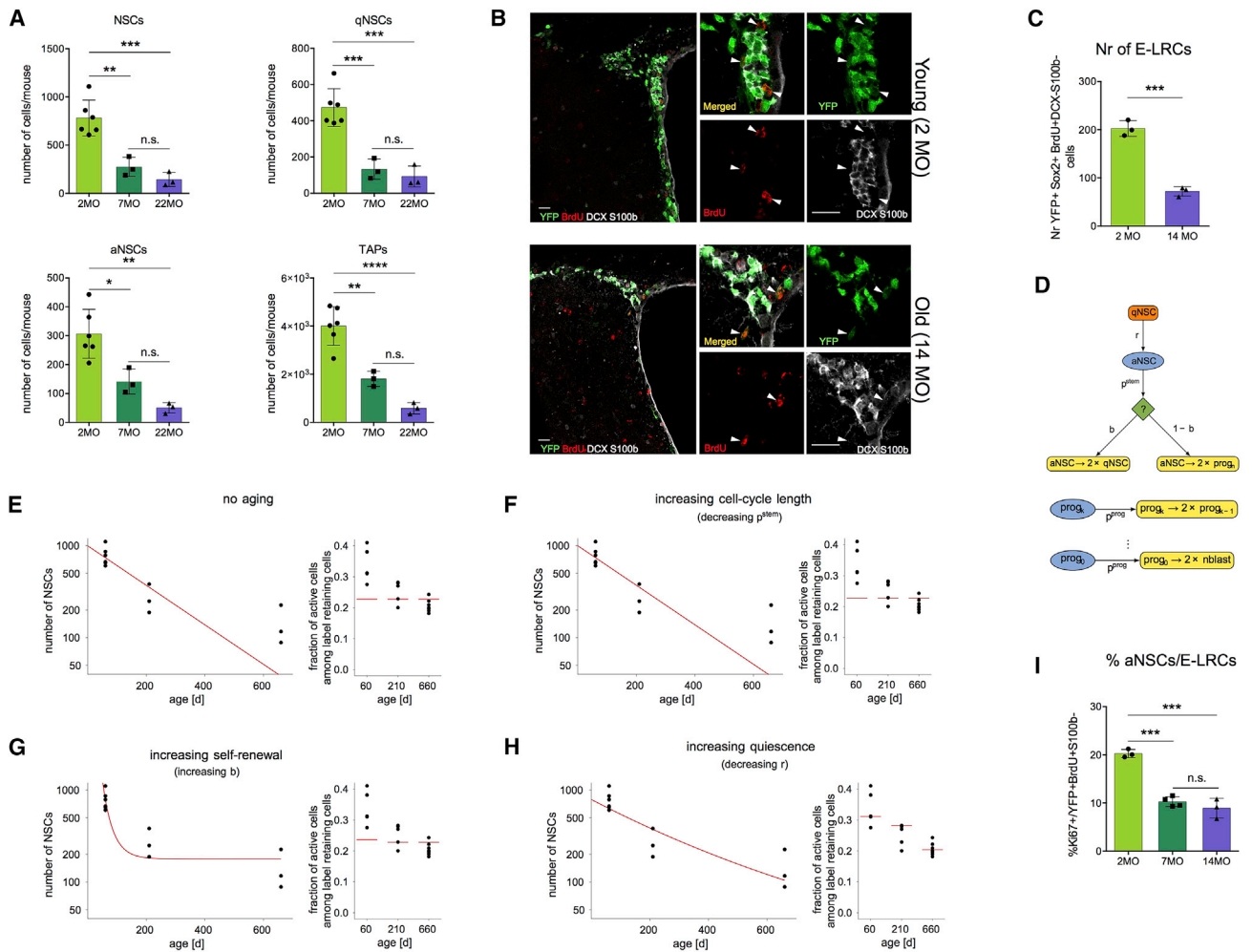
Figure 1. A Time-Dependent Increase in Quiescence Maintains a Stem Cell Reservoir at Old Age

(A) FACS analysis of total number of NSCs, qNSCs, aNSCs, and TAPs from both V-SVZs of mice of different ages (2 MO, n = 6 replicates of 2 pooled mice; 7 MO, n = 3 replicates of 2 pooled mice; 22 MO, n = 3 replicates of 3 pooled mice; bar and whiskers denote mean ± SD; Tukey-Kramer multiple-comparisons test).

(B) Representative pictures of 2 MO and 14 MO SVZ (scale bar, 20 μm; white arrows indicate E-LRCs).

(C) Quantification of total number of YFP$^+$Sox2$^+$BrdU$^+$DCX$^-$S100b$^-$ cells/SVZ/Section at 2 and 14 MO (n = 3 mice per group; bar and whiskers denote mean ± SD; Student's t test).

(D) Schematic representation of MM. qNSCs can enter the cell cycle to become aNSCs. aNSCs divide to either produce two qNSCs or two TAPs (progn). Progenitors have the capacity of n symmetric self-renewing divisions, which give rise to neuroblasts (nblast).

(E–H) Fit of neurogenesis model to the data assuming no aging (E), cell-cycle lengthening (F), increasing self-renewal (G), or increasing quiescence (H) (red represents model and black experimental data).

(I) Quantification of fraction of Ki67$^+$ among YFP$^+$Sox2$^+$BrdU$^+$S100b$^-$ cells at 2, 7, and 14 MO (n = 3 mice per group; bar and whiskers denote mean ± SD; Tukey-Kramer multiple-comparisons test). *p < 0.05; **p < 0.01; ***p < 0.001; n.s., not significant.

See also Figures S1 and S5, Table S6, and Data S1.

activation from quiescence). This prediction was experimentally validated by the significant decrease of the percentage of aNSCs among E-LRCs between 2, 7, and 14 MO (Figures 1I and S1G). Altogether, these data show that during homeostasis, the fraction of NSCs in quiescence increases with age.

We next asked if qNSCs are equally able to become activated upon injury in the young and old brain. To this end, we ablated cycling cells including aNSCs, TAPs, and neuroblasts (NBs) using temozolomide (TMZ), a DNA-alkylating agent (Figure 2A).

This ablation activates qNSCs to replenish the NSC compartment (Mich et al., 2014). Proliferation of V-SVZ NSCs in 2 and 22 MO mice was assessed by a 2-h BrdU labeling protocol at 0, 1, 9, and 35 days following TMZ treatment (Figures S2A and S5). 35 days following TMZ treatment, the number of aNSCs rose again to approximately the same level as before (92% of the cell number after the control treatment; 95% confidence interval [CI] according to Student's t test: 67%–117%) in young mice, while only 44% (95% CI: 37%–51%; p = 2.7*10−5) of
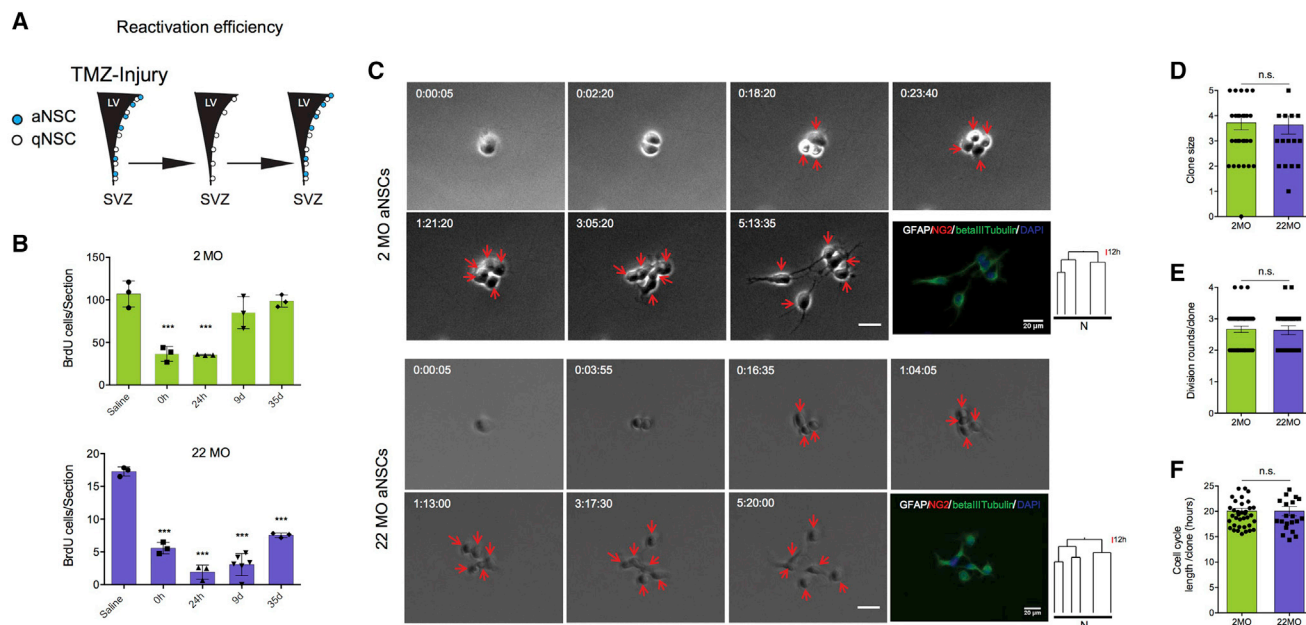
Cell

Figure 2. qNSCs Are Resistant to Activation While aNSCs Exhibit Similar Behavior in the Young and Old Brain

(A) Schematic representation of experimental setup.

(B) Quantification of BrdU$^+$ cells/SVZ/section in 2 MO and 22 MO mice (each data point represents a mouse; bar and whiskers denote mean ± SD; Tukey-Kramer multiple-comparisons test; statistics compared to the control group).

(C) Phase contrast time-lapse microscopy pictures of sorted 2 MO and 22 MO aNSCs for 5 days. (day:h:min). Post-imaging immunocytochemistry for GFAP (white), NG2 (red), and βIII-tubulin (green) and lineage tree for the depicted clones (scale bar, 20 μm).

(D) Average clone size of dividing cells.

(E) Average number of division rounds per clone.

(F) Average cell-cycle length per clone (2 MO n = 39 clones, 22 MO n = 21 clones; bar and whiskers denote mean ± SEM). ***p < 0.001; n.s., not significant.

See also Figures S2, S5, and S6.

the control level was achieved in old mice (Figure 2B). Hence, old qNSCs are more resistant to injury-induced activation and thus unable to quickly repair the old brain.

Young and Old NSCs Are Functionally and Molecularly Similar

We next set out to address the factors involved in the NSCs' resistance to enter the activation state. DNA damage increases upon aging in several stem cell compartments (Oh et al., 2014), potentially compromising their function. This is the case for quiescent hematopoietic stem cells (HSCs) that exhibit DNA damage upon repeated activation, as assessed by the alkaline comet assay (Walter et al., 2015). However, the comet assay on freshly sorted qNSCs and aNSCs from young and old mice revealed no major differences in the levels of DNA damage (Figures S2B, S2C, and S6). We next tested if once activated, old and young NSCs would perform different. To this end, we recorded the cell dynamics of freshly sorted active NSCs from 2 and 22 MO mice via time-lapse video microscopy for a period of 6 days and reconstructed their lineage trees (Figures 2C and S2D). In the absence of growth factors or other extrinsic signals, aNSCs follow their *in vivo* fate allowing evaluation of parameters such as clone size, rounds of division, and average cell-cycle length (Ortega et al., 2013). After several rounds of division, both young and old aNSCs gave rise to NBs demonstrating their

neurogenic potential (Figure 2C); both young and old aNSCs generated clones of similar size (Figure 2D), underwent similar number of division rounds (Figure 2E), and exhibited similar average cell-cycle length (Figure 2F). In addition, freshly sorted aNSCs from 2, 7, and 22 MO mice exhibited similar self-renewal capacity as assessed by an *in vitro* sphere assay (Figures S2E and S2F). Altogether, these results show that once activated, old NSCs perform as well as their younger counterparts.

We then investigated the molecular underpinnings of age-induced quiescence using single-cell transcriptomics data of 89 NSCs from 2 MO mice and 133 NSCs from 23 MO mice. These NSCs were sequenced using the Smart-seq2 protocol. Our analysis on NSCs from young mice has already been published (Llorens-Bobadilla et al., 2015; Figure S6A). Here, we used additional libraries from old mice that had also been prepared in the context of our previous study but not discussed there. When including these additional libraries, hierarchical clustering identified the four different activation states of NSCs (qNSC1, qNSC2, aNSC1, aNSC2) that we had previously reported (Table S1; Llorens-Bobadilla et al., 2015). Interestingly, principal component analysis revealed that the activation state, and not the age, is the dominant source of difference (Figures 3A and 3B). This result also confirms that there are at most only minimal batch effects between the young and the old dataset. Notably, the proportion of qNSCs was much higher among
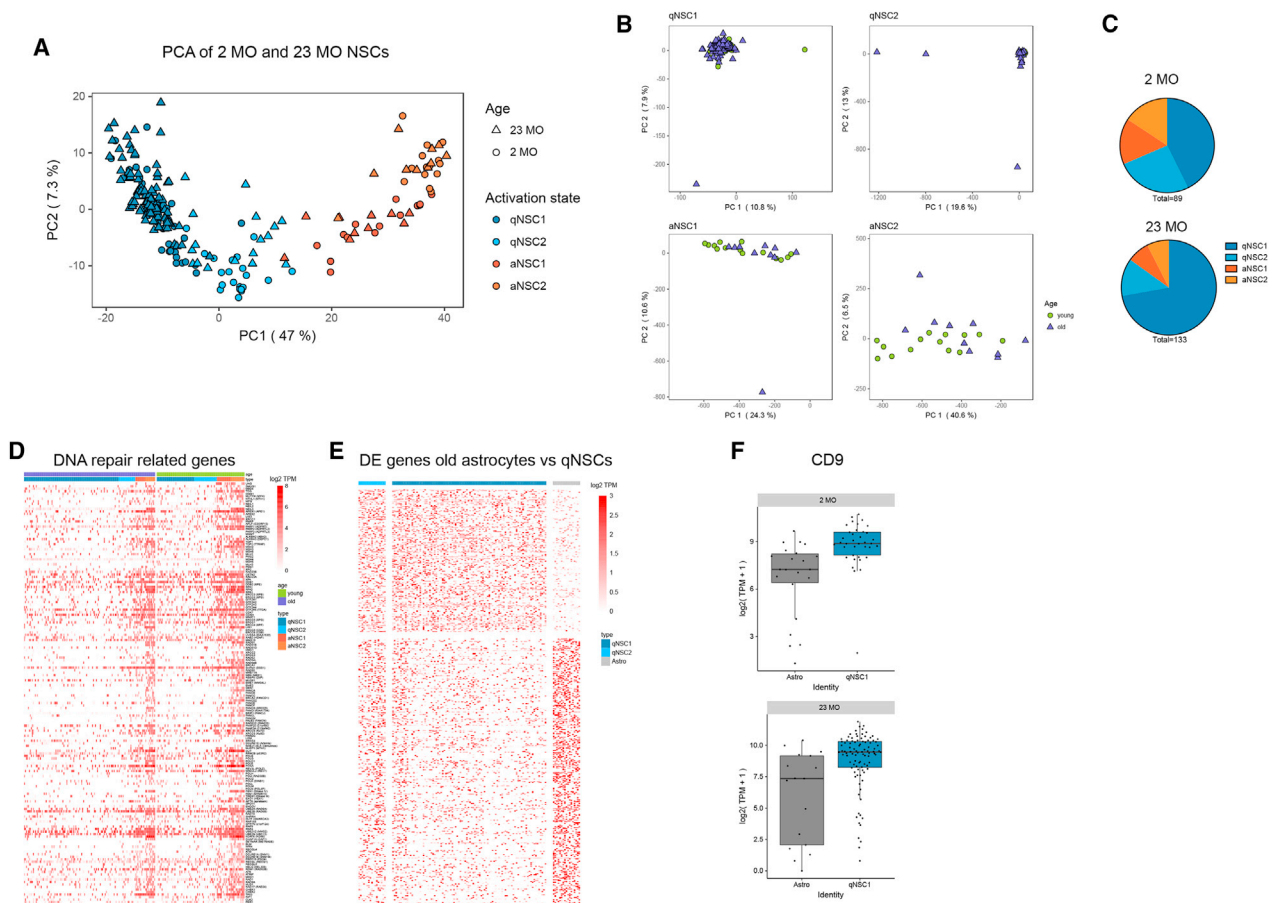
Figure 3. The Individual Transcriptomes of Young and Old NSCs (Smart-Seq2 Technology) Show an Increased Fraction of Old qNSCs

(A) PCA plot for the transcriptomes of 89 NSCs of 2 MO mice (circles) from Llorens-Bobadilla et al. (2015) and 133 NSCs of 23 MO (triangles). Colors indicate different activation states, as identified from the hierarchical clustering in Llorens-Bobadilla et al. (2015). See Table S1.

(B) PCA plots of individual subpopulations of NSCs sequenced with the Smart-seq2 protocol. Green dots, cells from 2 MO; purple triangles, cells from 23 MO mice.

(C) Pie charts representing the fraction of NSCs in different activation states from 2 and 23 MO mice.

(D) Heatmap of manually selected genes involved in DNA damage-response pathways.

(E) Log2-transformed TPM gene expression values of all the DE genes (with absolute log fold change >1 and p < 0.01) between old qNSC1 and astrocytes, shown for qNSC1, qNSC2 cells, and astrocytes from the Smart-seq2 data. Top half: upregulated genes that are expressed higher in qNSC1s than in astrocytes. Bottom half: downregulated genes that are expressed lower in qNSC1s than in astrocytes. See Table S2.

(F) Boxplots of CD9 expression in astrocytes and qNSC1 cells from 2 and 23 MO mice (likelihood ratio test, adjusted p value <0.003).

See also Figures S3 and S6 and Table S4.

NSCs from old mice than in those from young mice (Figure 3C). Interestingly, the expression of DNA repair-related genes was higher in aNSCs versus qNSCs irrespective of age (Figure 3D). To ensure that the much higher number of qNSC1 is not due to contaminating astrocytes, we additionally sequenced cortical and striatal astrocytes from old mice. We found many differentially expressed (DE) genes between astrocytes and qNSC1. Among these DE genes, CD9, a marker previously shown to be higher expressed in NSCs than in astrocytes (Llorens-Bobadilla et al., 2015; Figures 3E and 3F; Table S2). These data suggest that the increased number of cells within the qNSC1 cluster is not due to mislabeling of contaminating astrocytes but to a higher number of bona-fide qNSC1 profiles in the aging brain.

To sequence a higher number of cells, we used the Chromium Single Cell 3′ platform from 10x Genomics (sequenced libraries were produced in an identical manner). To this end, we profiled a GLAST$^+$ fraction of V-SVZ cells enriched for NSCs from 2 and 22 MO mice (Figure S6B). 1,696 young and 1,370 old cells passed the quality control and were used for further analysis (Table S4). 9 different clusters were identified using the Seurat package (Figure 4A). We used genes expressed specifically in each cluster to assign them as qNSCs (qNSC1, qNSC2), aNSCs (aNSC0, aNSC1, aNSC2), TAPs, NBs, oligodendrocytes (ODs), and oligodendrocyte progenitors (OPCs) according to previously published classification (Basak et al., 2018; Dulken et al., 2017; Llorens-Bobadilla et al., 2015) (Figure 4A; Table S1). Complementary to the clustering analysis by Seurat, we used Monocle
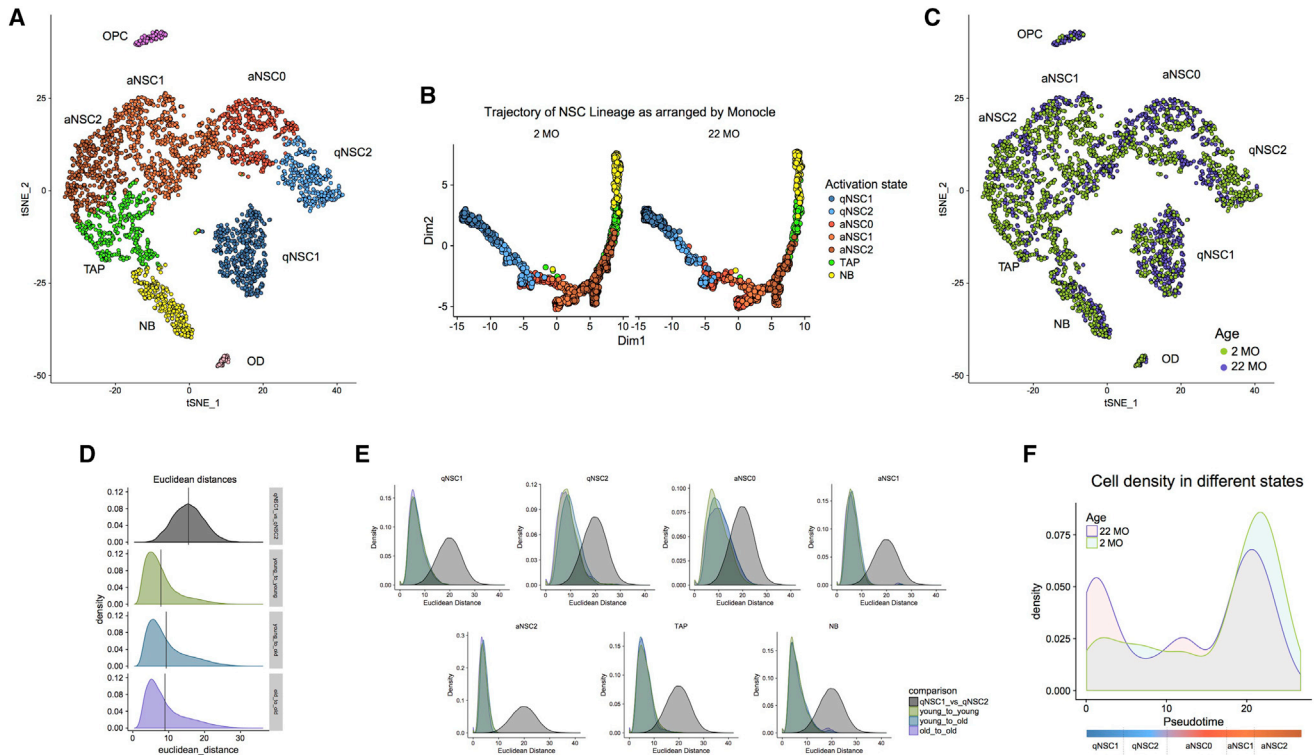
Cell

Figure 4. Single-Cell Transcriptomics (Chromium Cell 3′ Platform) Uncovers a Remarkable Similarity between Young and Old NSCs
(A) t-Distributed stochastic neighborhood embedding (t-SNE) of 1,696 cells from 2 MO and 1,370 cells from 22 MO mice. Colors indicate assigned activation states and cell types.
(B) Ordering of young and old single cell transcriptomes using monocle 2. The pseudotime order agrees with the assigned activation states.
(C) Same t-SNE map as in (A), with colors representing cells from 2 (green) and 22 MO (purple) mice. The good intermixing indicates absence of noticeable batch effects.
(D) Euclidean distance distributions of cells within a window of 5 pseudotime units comparing within and between cells originating from 2 and 22 MO animals. Euclidean distance between cells from qNSC1 and qNSC2 activation states within a pseudotime window of 5 units serves as reference. Lines denote the mean Euclidean distance observed.
(E) Comparison of Euclidean distance distributions between cells of the same activation state from young and old, young and young, and old and old mice (overlaid). Euclidean distance between qNSC1 and qNSC2 serves as reference.
(F) Density estimate of cell number along the pseudotime from qNSC1 to aNSC2 per age group.
See also Figures S3 and S6 and Tables S1 and S4.

2 to assign a linear "pseudotime" ordering to the cells (excluding ODs and OPCs). This analysis confirmed the same lineage progression from qNSCs1 → qNSCs2 → aNSCs0 → aNSCs1 → aNSCs2 → TAPs → NBs for old and young NSCs (Figures 4B and S3A). The t-distributed stochastic neighborhood embedding (t-SNE) plot gives the impression of a disconnection between qNSC1 and the rest of the continuum of neurogenesis; this, however, might be an artifact of the t-SNE projection. To test this, we inspected the distribution of Euclidean distances between cells within the qNSC1 and qNSC2 clusters and found them to be comparable to the qNSC2—aNSC0 distances but substantially lower than distances between distantly related clusters like qNSC1—mature ODs (Figure S3B). As previously observed in young NSCs, lineage transitions were accompanied by a continuous gradient of expression changes between the different stages (Figures S3C and S3D; Table S1). Altogether, comparison of young and old NSCs showed that they share the same activation states and proceed along the same lineage.

Surprisingly, only the activation state, but not the age of the cells, dictated their segregation to the different clusters (Figures 4C, S3A, and S3E). To assess in more depth the similarity of young and old transcriptomes, we calculated the Euclidean distance distributions of cells within a window of 5 pseudotime units comparing within and between cells originating from 2 and 22 MO animals. We observed similar distances within and between the age groups that were much lower than between qNSC1 and qNSC2 cells (Figure 4D). The same was observed for Euclidean distance distributions of cells within each separate cluster as compared to cells between qNSC1 and qNSC2 cluster for 10x and Smart-seq2 technologies (Figures 4E and S3F). This comparison, and the DE analysis of age-induced changes within each activation state (Figure S3F; Table S2), strongly indicates that age induces changes in fewer genes, as compared to changes induced by lineage transition. In addition, comparison of the average gene expression of young and old NSCs, or cells within the neurogenic lineage, revealed a much lower

number of genes showing expression changes higher than 2-fold than for the oligodendrocyte lineage (OD and OPCs) at young and old ages (Figure S3H).

While the transcriptome associated with a specific pseudo-time (i.e., position in the NSC continuum) does not change with age, the distribution of pseudotime assignment does. In line with the higher fraction of qNSCs in the old brain (discussed above), we observed an increase in pseudotime assignments to the early qNSC1 (Figure 4F). While young NSCs transit smoothly from a quiescent to a primed-quiescent state that is readily followed by activation, old NSCs remain in the dormant state (qNSC1), and fewer cells enter the aNSC0 state, to become fully activated (Figure 4F). Thus, the transcriptional profile of NSCs at different ages remains similar, but old NSCs tend to be in a quiescent state.

Niche Inflammatory Signals Keep Old NSCs in a Quiescent State

We therefore set out to search for niche-derived signals that could induce quiescence. To this end, we profiled different cell types residing within the V-SVZ niche including endothelial cells (ECs), microglia (Mg), NBs, and NSCs using bulk RNA sequencing from 2 and 19 MO mice (Figure S6C). Differential expression analysis revealed a common enriched expression of transcripts related to inflammatory response in every cell type (Figures 5A and 5B; Table S2). It also showed that ECs exhibit the highest age-related changes (Figure 5A). To explore when the onset of the inflammatory response occurs in NSCs, we also performed NSC bulk RNA sequencing from 7 MO mice, which revealed that inflammatory genes expression at 7 MO is already higher than in 2 MO mice (Figure 5C).

While inflammatory genes expression was captured with bulk RNA sequencing, the observed age-imposed transcriptional changes were mild to be reliably detected at the single cell level. Overall, the differences seen in bulk sequencing data are also partly visible in the single cell Smart-seq2 data for those genes that could be detected in a sufficiently large fraction of the cells (Figure S3G). Indeed, analysis of the read counts in single NSCs sequenced by either 10x 3' Chromium or Smart-seq2 technology, revealed that the inflammation signal is too weak and can only be detected by Smart-seq2 (in only few cells) but not by the 10x technology (Figure S3I; Table S2). Of note, basal expression of interferon response genes is already observed in young mice, which is suggestive of a role of interferons in NSC homeostasis. We next assessed the expression of the nuclear pro-inflammatory cytokine IL33, which has been reported to activate the innate immune response by inducing interferon production in the NSC compartment of 2 and 22 MO TLX-CreER^{T2}YFP mice. The proportion of IL33$^+$ NSCs changed from around 0.5% in the young V-SVZ to 15% in the old V-SVZ (Figures 5D and 5E). However, the NSC fraction that is retained in a quiescent state is much higher. Thus, we hypothesized that inflammatory cytokines derived from neighboring cells might contribute to induction of quiescence in the NSC compartment. Along this line, previous studies have shown that sustained inflammation activates Mg to reduce proliferation of neighboring NSCs in the young V-SVZ (Solano Fonseca et al., 2016). In addition, ECs already induce quiescence of NSCs in a non-inflammatory state

(Ottone et al., 2014). Accordingly, exposure of NSCs to inflammatory interferons (IFNα and INFβ) greatly reduced proliferation of NSCs in vitro (Figure 5F). To address the contribution of INFs to the age-dependent induction of quiescence, we examined the fraction of aNSCs among adult-LRCs in 2 and 22 MO IFNα and INFγ receptor-knockout mice (IFNAGRKO) (Figure S5A). We hypothesized that if inflammation, specifically INFs, are a main quiescence driver, their absence would result in NSC dynamics resembling the "no aging" scenario of our MM (Figure 1E). Consistent with the prediction of the "no aging" model, the fraction of aNSCs among LRCs did not change across time and was therefore significantly higher in old INF-deficient animals than in old wild-type counterparts (Figure 5G). Thus, neutralizing inflammation levels off the age-related decline in activation of V-SVZ NSCs at old ages.

Finally, we investigated whether an acute inflammation inhibition in the old V-SVZ niche could activate NSCs in the old brain. Previous reports had shown that the sole neutralization of the inflammatory cytokine CXCL10 greatly improves hippocampal synaptic plasticity in the context of an INF response triggered by a viral infection (Blank et al., 2016). Therefore, we decided to treat aged animals with a neutralizing antibody against CXCL10. Mini-osmotic pumps containing anti-CXCL10 or isotype control antibodies were implanted in the lateral ventricles of 22 MO mice, and BrdU was administered for 3 days. Olfactory bulb neurogenesis was assessed by quantification of newborn NBs 4 days later (Figure S5C). Notably, inhibition of CXCL10 significantly increased the number of NBs (Figure 5H). To confirm that this increase was due to activation of qNSCs, we administered BrdU in the drinking water for 14 days followed by a chase time of 21 days. Mini-osmotic pumps with anti-CXCL10 or isotype control antibodies were implanted 7 days before sacrificing the animals (Figure S5A). CXCL10 neutralization significantly decreased the number of LRCs compared to IgG-treated mice indicating activation of qNSCs (Figure 5I). Thus, inhibition of CXCL10 decreased the number of qNSCs, and increased the production of NBs during homeostasis providing a causal link between inflammation and induction of quiescence in the aged brain.

A Markov Chain Approach Identifies the Wnt Antagonist sFRP5 as an Additional Niche Signal Maintaining Quiescence

To identify additional age-related signals contributing to induction of NSC quiescence emanating from the niche we developed a Markov chain-based computational approach (MCCM) (Data S2). This approach aims at unveiling NSC-intrinsic signaling intermediates that are likely to maintain a specific cell state dictated by niche signals via a sustained effect on the downstream gene regulatory network (Ravichandran and Del Sol, 2017) (Figure 6A; Data S2). For this analysis, we used the Smart-seq2 single-cell expression data of qNSCs and aNSCs from young and old mice. This approach enabled identification of key signaling intermediates likely to be constantly active or inactive in a majority of cells in the respective cellular subpopulations, among them Bmpr1a, a regulator of NSC quiescence (Mira et al., 2010) (Table S3). We focused on intermediates identified as uniquely active in old NSCs. The method identified eight
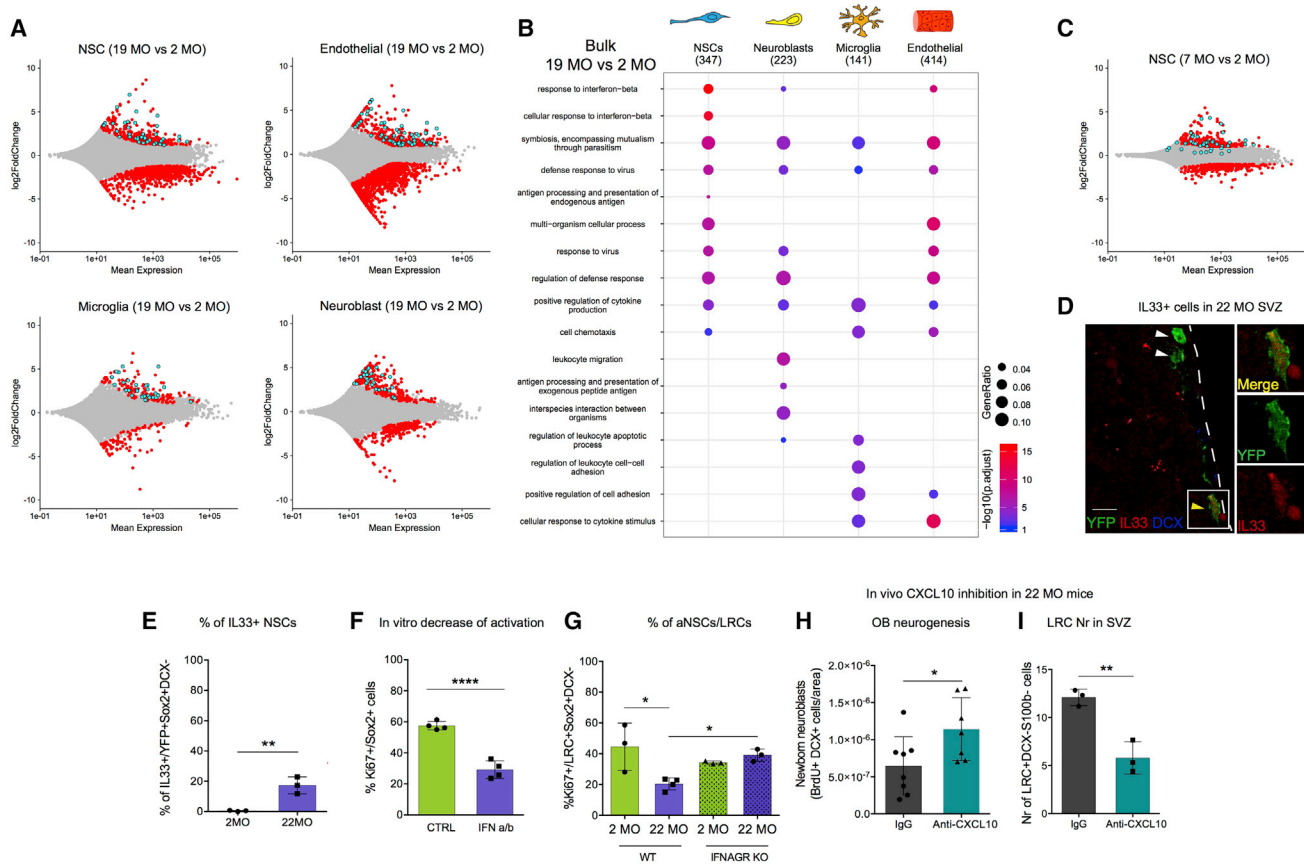
Cell

Figure 5. Niche Inflammatory Signals Keep Old NSCs in a Quiescent State

(A) Mean log2 fold change per gene in the comparison between 19 and 2 MO bulk samples (NSCs, ECs, Mg, and NB cells). Red dots represent significantly DE genes (adjusted p < 0.05, absolute log2 fold change >1). Blue dots represent significantly upregulated genes annotated as innate immune response genes by InnateDB (Breuer et al., 2013).

(B) Gene ontology analysis of genes upregulated upon aging (>2-fold change, p value <0.05) of bulk populations from different SVZ cell types. See Table S2.

(C) Mean log2 fold change per gene in the comparison between 7 versus 2 MO bulk sequencing samples of NSCs. Red dots represent significantly DE genes (adjusted p < 0.05, absolute log2 fold change >1). Blue dots represent significantly upregulated genes annotated as innate immune response genes by InnateDB (Breuer et al., 2013) from the comparison of 19 versus 2 MO.

(D) Representative picture of old SVZ immunostainings for IL33, YFP, and DCX (scale bar, 10 μm; white arrows indicate Il33$^-$ and yellow Il33$^+$ NSCs).

(E) Fraction of IL33$^+$ among YFP$^+$SOX2$^+$DCX$^-$ cells at 2 and 22 MO mice (n = 3 mice per group; bar and whiskers denote mean ± SD; Student's t test).

(F) Percent of Ki67$^+$ among Sox2$^+$ NSCs after 48 h of treatment with IFNα/β; (n = 4 primary cell lines; bar and whiskers denote mean ± SD; Student's t test).

(G) Percent of Ki67$^+$ among Sox2$^+$LRC$^+$DCX$^-$ NSCs in 2 MO and 22 MO WT and IFNAGR KO mice (n = 3 mice per group; bar and whiskers denote mean ± SD; Tukey-Kramer multiple-comparisons test).

(H) Number of DCX$^+$BrdU$^+$ cells arriving in the OB after CXCL10 inhibition normalized to the area (IgG n = 8 mice, anti-CXCL10 n = 7 mice; bar and whiskers denote mean ± SD; Student's t test).

(I) Number of LRCs (BrdU$^+$DCX$^-$S100b$^-$)/SVZ per section after CXCL10 inhibition (n = 3 mice per group; bar and whiskers denote mean ± SD; Student's t test).

*p < 0.05; **p < 0.01; ****p < 0.0001; n.s., not significant.

See also Figures S5 and S6.

genes uniquely expressed in old qNSC1 (Table S3). From these, we focused on *Sfrp5*, a known antagonist of the Wnt signaling pathway that was strongly expressed in old qNSCs (Figures S4A and S4B; Table S3). To address potential age-dependent changes in canonical Wnt-activity, we used TCF/Lef-H2B-GFP reporter mice that express an H2B-GFP fusion protein under the control of 6 TCF/Lef binding sites (Ferrer-Vaquer et al., 2010). We observed a higher fraction of GFP+NSCs among NSCs in the dorsal domain as compared to the latero-ventral domain of V-SVZ (Figures 6B–6D), in line with the previously described function of Wnt-canonical signaling in generation of oligodendrocyte lineage within the dorsal domain (Ortega et al., 2013). Ependymal cells, which lie along the entire wall of the lateral ventricles, were GFP-positive (Figure 6C). Importantly, the total number of GFP+NSCs significantly increased (1.4-fold) at 8 MO as compared to 2 MO (Figure 6D). Most DCX$^-$ Ki67$^+$ cells that can only be active NSCs or TAPs were TCF-LEF-negative indicating that canonical Wnt activity is high in qNSCs (Figures S4C and S4D). We hypothesized that sFRP5 antagonizes non-canonical Wnt activity thereby leading to increased
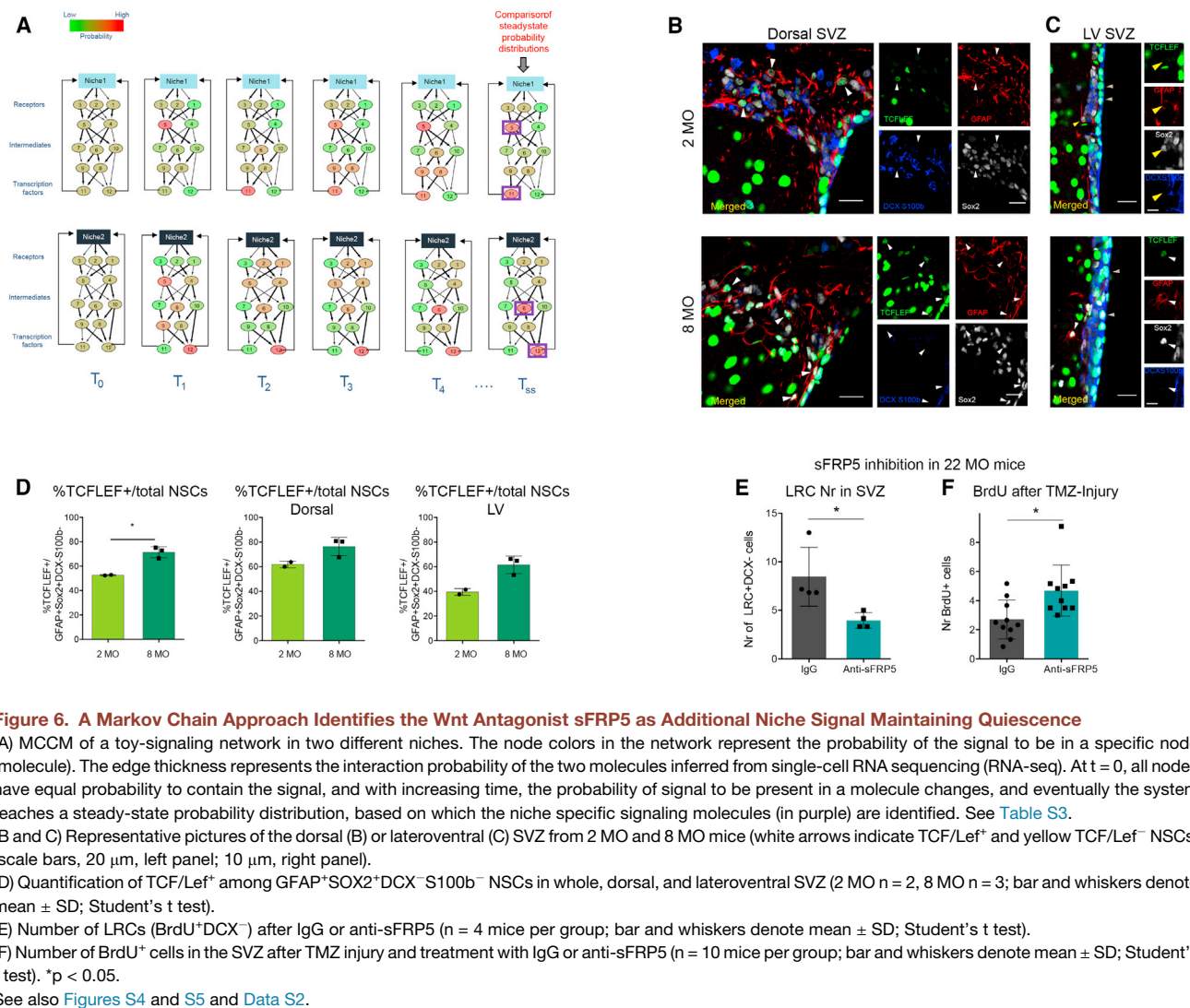
Figure 6. A Markov Chain Approach Identifies the Wnt Antagonist sFRP5 as Additional Niche Signal Maintaining Quiescence

(A) MCCM of a toy-signaling network in two different niches. The node colors in the network represent the probability of the signal to be in a specific node (molecule). The edge thickness represents the interaction probability of the two molecules inferred from single-cell RNA sequencing (RNA-seq). At t = 0, all nodes have equal probability to contain the signal, and with increasing time, the probability of signal to be present in a molecule changes, and eventually the system reaches a steady-state probability distribution, based on which the niche specific signaling molecules (in purple) are identified. See Table S3.

(B and C) Representative pictures of the dorsal (B) or lateroventral (C) SVZ from 2 MO and 8 MO mice (white arrows indicate TCF/Lef$^+$ and yellow TCF/Lef$^-$ NSCs) (scale bars, 20 μm, left panel; 10 μm, right panel).

(D) Quantification of TCF/Lef$^+$ among GFAP$^+$SOX2$^+$DCX$^-$S100b$^-$ NSCs in whole, dorsal, and lateroventral SVZ (2 MO n = 2, 8 MO n = 3; bar and whiskers denote mean ± SD; Student's t test).

(E) Number of LRCs (BrdU$^+$DCX$^-$) after IgG or anti-sFRP5 (n = 4 mice per group; bar and whiskers denote mean ± SD; Student's t test).

(F) Number of BrdU$^+$ cells in the SVZ after TMZ injury and treatment with IgG or anti-sFRP5 (n = 10 mice per group; bar and whiskers denote mean ± SD; Student's t test). *p < 0.05.

See also Figures S4 and S5 and Data S2.

canonical activity and thus quiescence in the aging brain. Thus, we tested if neutralization of sFRP5 could decrease quiescence in old NSCs by administering a neutralizing antibody against human sFRP5 *in vivo*. We confirmed that this antibody was able to recognize mouse recombinant sFRP5 *in vitro* and able to block Wnt3a-mediated activity in a TOPFLASH assay (Figure S4E). Thereafter, we used the LRC protocol followed by a chase time of 8 weeks and implanted mini-osmotic pumps containing anti-sFRP5 or isotype control antibodies 14 days before sacrificing the animals (Figure S5A). We observed a significantly decreased number of LRCs following sFRP5 inhibition as compared to IgG-treated control old mice (Figure 6E). We thereafter tested the effect of sFRP5 inhibition in NSC-mediated repair of the injured niche. To this end, we challenged the animals with TMZ and implanted mini-osmotic pumps 6 days before sacrificing them (Figure S5B). sFRP5 inhibition significantly increased the number of proliferating cells, as assessed by a 2-h BrdU labeling protocol, in old mice as compared to IgG-treated control old mice (Figure 6F). Thus, neutralization of sFRP5 can release the brake on

NSC activation in the old brain during homeostasis but also following injury.

DISCUSSION

A Role of Quiescence in Preserving a Reservoir of Stem Cells in the Aged Brain

Although previous studies had already reported a shrinkage of the V-SVZ NSC pool with age (Ahlenius et al., 2009; Obernier et al., 2018; Shook et al., 2012; Silva-Vargas et al., 2016), others have reported no age-related changes (Daynac et al., 2016). This study confirms that the pool of adult V-SVZ-NSCs exhibits an age-dependent depletion, using three independent methods: counting marker-positive cells by FACS and immunostainings of embryonic and adult LRCs of the young and old V-SVZ. As previously hypothesized (Obernier et al., 2018), and as confirmed by the "no-aging" scenario of our mathematical modeling, the fact that NSCs have a higher probability to differentiate than to undergo self-renewing divisions leads to a

Cell

time-dependent attrition. Indeed, without an age-dependent increase in the fraction of qNSCs, NSCs would undergo full depletion in the old brain. This prediction does not exclude an additional contribution of changes in other parameters but reveals that changes in "time-in-quiescence" are the only parameter that allows reproducing of the data on its own. Furthermore, allowing time-dependent changes in quiescence and self-renewal revealed that even if the two parameters undergo age-dependent changes, it is the time-increasing quiescence (decreasing rate of activation from quiescence) which is the major component of the regulatory process and explains the observed dynamics. Notably, models accounting for other transitions, such as asymmetric divisions of the form aNSC → progenitor + qNSC, or models assuming co-existence of both types of divisions, additional cell death, or direct fate transitions into astrocytes (Ziebell et al., 2018), yield the same conclusion, which indicates the universality of aging-induced quiescence. Accordingly, a lower fraction of LRCs that become reactivated in the aging brain have been independently detected through ultra-structural analysis of V-SVZ NSC following incorporation of radioactive thymidine (Capilla-Gonzalez et al., 2014).

Contrary to the present study, others have reported an age-dependent increase of cell-cycle length (Daynac et al., 2016). Daynac et al. (2016) detected a higher fraction of cells claimed to be in G1 state in the aging brain using FUCCI-reporter mice. Unfortunately, this reporter line cannot distinguish between G1 or G0, and thus, the data could be interpreted as increased cell-cycle length (of G1) as done by the authors or as an increased number of cells in a quiescent state (G0). In summary, our study reveals that, upon aging, a higher fraction of NSCs are found in quiescence, and this is a compensatory mechanism to avoid full depletion of the NSC compartment.

In addition, and as opposed to the concept of malfunctioning aged stem cells, our study reveals that once activated, old NSCs perform as well as younger counterparts in undergoing several rounds of division and generating clones with similar numbers of neurons. This is also demonstrated by similar levels of DNA damage in young and old NSCs, contrary to the higher levels reported in HSCs following chronic inflammation (Walter et al., 2015). Likewise, analysis of single-cell and bulk transcriptomes of old and young NSCs reveals that the large-scale transcriptional activity of the cells is given by their metabolic state, and age induces milder transcriptional changes that suffice to block transition from a quiescence to an active state. This study suggests that age globally changes the neurogenic niche, which impairs NSC activation. Once NSCs become activated, they function as well as young NSCs.

Inflammatory Signals from the Niche Impose Quiescence

The fraction of qNSCs in the old brain is not only increased, but is also more resistant to exiting quiescence even if forced by injury. Resistance to become activated has been shown only *in vitro* so far and it was linked to defects in lysosomal clearance in old NSCs (Leeman et al., 2018). However, we found a link of quiescence to inflammation. Inhibition of the INF response through deletion of INFα and INFγ led to a similar fraction of aNSCs in young and old V-SVZ. Importantly, these kinetics of the fraction

of aNSCs in young and old INF receptor-deficient mice was predicted by the "no-aging" scenario.

We have previously found that activation of INFγ response is required to increase activation of young NSCs upon injury (Llorens-Bobadilla et al., 2015). The opposing function of INFγ in injured young NSCs might be due to the duration of exposure to INF, which is acute for injury versus chronic for exposure in aging, or to the prevalence of INFα/INFβ activity in aging versus INFγ in injury. INFs derived from the choroid plexus had been reported to negatively impact adult hippocampal neurogenesis in the old brain (Baruch et al., 2014). However, how INFs decrease *de novo* generation of neurons was not addressed.

Our study underlines the importance of the niche for induction of quiescence. An age-dependent expression of transcripts related to inflammatory response is globally detected in the old niche, suggestive of a major contribution of the niche in induction of NSCs quiescence. Accordingly, models of heterochronic parabiosis have identified an age-related increase of systemic inflammatory factors, such as the cytokine CCL11, which are detrimental for hippocampal neurogenesis and cognitive functions (Villeda et al., 2011). Similarly, GDF11 was identified as a systemic factor that "rejuvenates" the aged V-SVZ (Katsimpardi et al., 2014). It would be interesting to address if the rejuvenating effect by this systemic factor is due to inhibition of quiescence. Interestingly, increased INF response was also detected in human aging brains (Baruch et al., 2014). In summary, our study establishes a causal link between inflammation and quiescence and shows that an early gain of quiescence would decrease the fraction of aNSCs at young age that then would be maintained at old age. In addition, an acute inhibition of inflammation at old age can help increasing *de novo* neuronal production in the old brain. Along this line, the difficulties in finding newborn neurons in the adult human brain (Kempermann et al., 2018) might be explained by the increased quiescence of adult human stem cells.

Control of Wnt Activity by the Niche through sFRP5

Finally, application of a Markov chain-based computational approach that aimed at discovering niche signals maintaining old NSCs in quiescent state identified the Wnt antagonist sFRP5. Modulation of two other Wnt antagonists, DKK1 and sFRP3, has been reported to control expansion of hippocampal NSCs in the young and old brain (Jang et al., 2013; Seib et al., 2013). Notably, our mathematical modeling of NSC dynamics in the hippocampus predicted that neutralization of DKK1 increases the generation of neurons in the aging brain by increasing the time in quiescence (Ziebell et al., 2018). Importantly, DKK1 antagonizes canonical Wnt signaling, as opposed to sFRP5 that putatively antagonizes non-canonical Wnt signaling, which suggest that in both neurogenic niches, the switch from canonical to non-canonical is required to enter the activation state. Zhu et al. (2014) detected decreased canonical Wnt activity in the old V-SVZ as compared to younger counterparts. This study used an Axin2-βGal reporter as read out for canonical Wnt signal and did not specifically address its expression in NSCs, but did in the whole V-SVZ tissue. As we show now, NSC Axin2 expression is masked by the highest expression in the ependymal compartment. Using a TCF/Lef reporter, we

found that canonical Wnt activity was majorly found in Ki67-negative cells, and thus, qNSCs. We hypothesize that a switch to non-canonical Wnt activity is required to enter activation at all ages, but in the aging V-SVZ, this activity can be inhibited by sFRP5. Accordingly, we show that an acute block of sFRP5 increased the fraction of actively cycling NSCs in the old brain following homeostasis and a temozolomide injury. Likewise, inhibition of canonical Wnt activity in the old bone improved bone healing (Baht et al., 2015). In the hematopoietic system, however, a detrimental increase of non-canonical Wnt signaling was found in aged HSCs (Florian et al., 2013). In summary, Wnt activity, either canonical or non-canonical, crucially regulates activation of adult somatic stem cells. Importantly, a link between Wnt activity and inflammation has been speculated in the old and the injured brain (Marchetti and Pluchino, 2013). A good example is Mg that use non-canonical or canonical Wnt activity to respectively activate or inhibit expression of inflammatory cytokines (Marchetti and Pluchino, 2013). Also, inflamed Mg decrease NSC proliferation and neuronal production (Solano Fonseca et al., 2016). Thus, we speculate that increased expression of the non-canonical Wnt inhibitor increases inflammatory signals from niche cells such as Mg, which consequently leads to reduced activation of NSCs. This would explain why blocking inflammation or expression of sFRP5 would similarly lead to increased exit of quiescence in old NSCs.

In summary, this study reveals that quiescence induction is used to preserve a small pool of NSCs in the old brain. Aged NSCs perform as well as their younger counterparts once activated but are more resistant to becoming activated. Analysis of the bulk or individual transcriptomes of NSCs shows that transitions throughout the different activation states are underlined by profound transcriptional changes in metabolism-related programs that can be readily detected at the single-cell level. However, age-related transcriptional changes are too mild to be reliably detected at the single-cell level and could only be detected by bulk-sequencing or predicted by the Markov chain approach. In addition, this study reveals a causal link between maintenance of quiescence, inflammation, and non-canonical Wnt activity. Understanding how to modulate the balance between quiescence and activation of NSCs in the old brain will be critical to preserve stem cell function in the aging brain.

STAR★METHODS

Detailed methods are provided in the online version of this paper and include the following:

- KEY RESOURCES TABLE
- CONTACT FOR REAGENT AND RESOURCE SHARING
- EXPERIMENTAL MODEL AND SUBJECT DETAILS
  - Mouse strains
- METHOD DETAILS
  - Implantation of mini-osmotic pumps
  - BrdU
  - Temozolomide (TMZ) treatment
  - Tamoxifen
  - Treatments with neutralizing antibodies
  - FACS analysis and sorting
  - Time-lapse video microscopy
  - Immunostainings
  - Cells
  - Isolation and cultivation of NSCs *in vitro*
  - Luciferase Reporter (Topflash) assays
  - Sphere assay
  - Comet assay
  - Microscopy
  - Analysis of Smart-seq2 single-cell RNA-seq data
  - Read trimming and mapping
  - RNA-seq data quality metrics
  - Gene Expression Matrices
  - Quality control of single-cell RNA-seq data
  - ERCC spike-in controls
  - Monocle pseudotime assignment
  - Expression of DNA damage associated genes
  - PCA
  - DE analysis Smart-seq2
  - Euclidean distance calculation
  - Bulk RNA sequencing
  - GO term enrichment analysis
  - Expression of Innate immune response genes
  - 10x Chromium 3′sequencing
  - Analysis with the Seurat package
  - Monocle pseudotime assignment
  - DE and GO term enrichment analysis
  - Euclidean distance calculation
- QUANTIFICATION AND STATISTICAL ANALYSIS
- DATA AND SOFTWARE AVAILABILITY

SUPPLEMENTAL INFORMATION

Supplemental Information includes six figures, four tables, and two data files and can be found with this article online at https://doi.org/10.1016/j.cell.2019.01.040.

ACKNOWLEDGMENTS

AUTHOR CONTRIBUTIONS

Acquisition, Analysis, and Interpretation of Experimental Data, G.K.; Bioinformatic Analysis of scRNa-seq, S.A., D.B., and S.Z.; Mathematical Model of NSC Dynamics, A.M.-C., F.Z., and T.S.; Markov Chain-Based Computation Approach, S.R. and A.D.; Acquisition of Cell Counts Used in the MM, F.C.-M. and J.K.; Assistance in Animal Experiments, S.L.; Inflammation-Related Data, J.B.; Smart-Seq2 RNA-seq of Young NSCs, E.L.-B.; Single-Cell 3′ Platform Libraries: K.B. and J.P.M.; Time-Lapse Lineage Tracing, B. Berninger and W.F.; Top Flash Assay, B. Berger; CXCL10 antibody, U.C.; Comet Assay, P.S.; Supervision, A.M.-V., A.M.-C., S.A., A.D., and B. Berninger; Writing & Editing, A.M.-V., G.K., A.M.-C., S.A., A.D.S., and B. Berninger; Project Conceptualization, A.M.-V. and G.K.; Project Design and Oversight, A.M.-V.

Cell

DECLARATION OF INTERESTS

The authors declare no competing interests.

SUPPORTING CITATIONS

The following references appear in the Supplemental Information: Burnham and Anderson (2002), Calzolari et al. (2015), Lim and Alvarez-Buylla (2016); Liu et al. (2016); Ponti et al. (2013); Rezza et al. (2014); Stewart (1994); Stiehl and Marciniak-Czochra (2011).

REFERENCES

Ahlenius, H., Visan, V., Kokaia, M., Lindvall, O., and Kokaia, Z. (2009). Neural stem and progenitor cells retain their potential for proliferation and differentiation into functional neurons despite lower number in aged brain. J. Neurosci. 29, 4408–4419.

Baht, G.S., Silkstone, D., Vi, L., Nadesan, P., Amani, Y., Whetstone, H., Wei, Q., and Alman, B.A. (2015). Exposure to a youthful circulaton rejuvenates bone repair through modulation of β-catenin. Nat. Commun. 6, 7131.

Baruch, K., Deczkowska, A., David, E., Castellano, J.M., Miller, O., Kertser, A., Berkutzki, T., Barnett-Itzhaki, Z., Bezalel, D., Wyss-Coray, T., et al. (2014). Aging. Aging-induced type I interferon response at the choroid plexus negatively affects brain function. Science 346, 89–93.

Basak, O., Krieger, T.G., Muraro, M.J., Wiebrands, K., Stange, D.E., Frias-Aldeguer, J., Rivron, N.C., van de Wetering, M., van Es, J.H., van Oudenaarden, A., et al. (2018). Troy+ brain stem cells cycle through quiescence and regulate their number by sensing niche occupancy. Proc. Natl. Acad. Sci. USA 115, E610–E619.

Berger, B.S., Acebron, S.P., Herbst, J., Koch, S., and Niehrs, C. (2017). Parkinson's disease-associated receptor GPR37 is an ER chaperone for LRP6. EMBO Rep. 18, 712–725.

Blank, T., Detje, C.N., Spieß, A., Hagemeyer, N., Brendecke, S.M., Wolfart, J., Staszewski, O., Zöller, T., Papageorgiou, I., Schneider, J., et al. (2016). Brain endothelial- and epithelial-specific interferon receptor chain 1 drives virus-induced sickness behavior and cognitive impairment. Immunity 44, 901–912.

Breuer, K., Foroushani, A.K., Laird, M.R., Chen, C., Sribnaia, A., Lo, R., Winsor, G.L., Hancock, R.E.W., Brinkman, F.S.L., and Lynn, D.J. (2013). InnateDB: systems biology of innate immunity and beyond–recent updates and continuing curation. Nucleic Acids Res. 41, D1228–D1233.

Burnham, K.P., and Anderson, D.R. (2002). Model Selection and Multimodel Inference: a Practical Information-Theoretic Approach (Springer).

Calzolari, F., Michel, J., Baumgart, E.V., Theis, F., Götz, M., and Ninkovic, J. (2015). Fast clonal expansion and limited neural stem cell self-renewal in the adult subependymal zone. Nat. Neurosci. 18, 490–492.

Capilla-Gonzalez, V., Cebrian-Silla, A., Guerrero-Cazares, H., Garcia-Verdugo, J.M., and Quiñones-Hinojosa, A. (2014). Age-related changes in astrocytic and ependymal cells of the subventricular zone. Glia 62, 790–803.

Daynac, M., Morizur, L., Chicheportiche, A., Mouthon, M.-A., and Boussin, F.D. (2016). Age-related neurogenesis decline in the subventricular zone is associated with specific cell cycle regulation changes in activated neural stem cells. Sci. Rep. 6, 21505.

Dobin, A., Davis, C.A., Schlesinger, F., Drenkow, J., Zaleski, C., Jha, S., Batut, P., Chaisson, M., and Gingeras, T.R. (2013). STAR: ultrafast universal RNA-seq aligner. Bioinformatics 29, 15–21.

Dulken, B.W., Leeman, D.S., Boutet, S.C., Hebestreit, K., and Brunet, A. (2017). Single-cell transcriptomic analysis defines heterogeneity and transcriptional dynamics in the adult neural stem cell lineage. Cell Rep. 18, 777–790.

Ernst, A., Alkass, K., Bernard, S., Salehpour, M., Perl, S., Tisdale, J., Possnert, G., Druid, H., and Frisén, J. (2014). Neurogenesis in the striatum of the adult human brain. Cell 156, 1072–1083.

Ferrer-Vaquer, A., Piliszek, A., Tian, G., Aho, R.J., Dufort, D., and Hadjantonakis, A.-K. (2010). A sensitive and bright single-cell resolution live imaging reporter of Wnt/ß-catenin signaling in the mouse. BMC Dev. Biol. 10, 121.

Florian, M.C., Nattamai, K.J., Dörr, K., Marka, G., Überle, B., Vas, V., Eckl, C., Andrä, I., Schiemann, M., Oostendorp, R.A.J., et al. (2013). A canonical to non-canonical Wnt signalling switch in haematopoietic stem-cell ageing. Nature 503, 392–396.

Fuentealba, L.C., Rompani, S.B., Parraguez, J.I., Obernier, K., Romero, R., Cepko, C.L., and Alvarez-Buylla, A. (2015). Embryonic origin of postnatal neural stem cells. Cell 161, 1644–1655.

Haas, B.J., Papanicolaou, A., Yassour, M., Grabherr, M., Blood, P.D., Bowden, J., Couger, M.B., Eccles, D., Li, B., Lieber, M., et al. (2013). De novo transcript sequence reconstruction from RNA-seq using the Trinity platform for reference generation and analysis. Nat. Protoc. 8, 1494–1512.

Hilsenbeck, O., Schwarzfischer, M., Skylaki, S., Schauberger, B., Hoppe, P.S., Loeffler, D., Kokkaliaris, K.D., Hastreiter, S., Skylaki, E., Filipczyk, A., et al. (2016). Software tools for single-cell tracking and quantification of cellular and molecular properties. Nat. Biotechnol. 34, 703–706.

Huang, S., Hendriks, W., Althage, A., Hemmi, S., Bluethmann, H., Kamijo, R., Vilcek, J., Zinkernagel, R.M., and Aguet, M. (1993). Immune response in mice that lack the interferon-gamma receptor. Science 259, 1742–1745.

Jacquet, B.V., Salinas-Mondragon, R., Liang, H., Therit, B., Buie, J.D., Dykstra, M., Campbell, K., Ostrowski, L.E., Brody, S.L., and Ghashghaei, H.T. (2009). FoxJ1-dependent gene expression is required for differentiation of radial glia into ependymal cells and a subset of astrocytes in the postnatal brain. Development 136, 4021–4031.

Jang, M.-H., Bonaguidi, M.A., Kitabatake, Y., Sun, J., Song, J., Kang, E., Jun, H., Zhong, C., Su, Y., Guo, J.U., et al. (2013). Secreted frizzled-related protein 3 regulates activity-dependent adult hippocampal neurogenesis. Cell Stem Cell 12, 215–223.

Katsimpardi, L., Litterman, N.K., Schein, P.A., Miller, C.M., Loffredo, F.S., Wojtkiewicz, G.R., Chen, J.W., Lee, R.T., Wagers, A.J., and Rubin, L.L. (2014). Vascular and neurogenic rejuvenation of the aging mouse brain by young systemic factors. Science 344, 630–634.

Kempermann, G., Gage, F.H., Aigner, L., Song, H., Curtis, M.A., Thuret, S., Kuhn, H.G., Jessberger, S., Frankland, P.W., Cameron, H.A., et al. (2018). Human adult neurogenesis: evidence and remaining questions. Cell Stem Cell 23, 25–30.

Kong, Y. (2011). Btrim: a fast, lightweight adapter and quality trimming program for next-generation sequencing technologies. Genomics 98, 152–153.

Leeman, D.S., Hebestreit, K., Ruetz, T., Webb, A.E., McKay, A., Pollina, E.A., Dulken, B.W., Zhao, X., Yeo, R.W., Ho, T.T., et al. (2018). Lysosome activation clears aggregates and enhances quiescent neural stem cell activation during aging. Science 359, 1277–1283.

Lim, D.A., and Alvarez-Buylla, A. (2016). The adult ventricular-subventricular zone (v-svz) and olfactory bulb (ob) neurogenesis. Cold Spring Harb. Perspect. Biol. 8, a018820.

Liu, H.K., Belz, T., Bock, D., Takacs, A., Wu, H., Lichter, P., Chai, M., and Schütz, G. (2008). The nuclear receptor tailless is required for neurogenesis in the adult subventricular zone. Genes Dev. 22, 2473–2478.

Liu, Y., Beyer, A., and Aebersold, R. (2016). On the dependency of cellular protein levels on mRNA abundance. Cell 165, 535–550.

Llorens-Bobadilla, E., Zhao, S., Baser, A., Saiz-Castro, G., Zwadlo, K., and Martin-Villalba, A. (2015). Single-cell transcriptomics reveals a population of dormant neural stem cells that become activated upon brain injury. Cell Stem Cell 17, 329–340.

Marchetti, B., and Pluchino, S. (2013). Wnt your brain be inflamed? Yes, it Wnt!. Trends Mol. Med. 19, 144–156.

Mich, J.K., Signer, R.A., Nakada, D., Pineda, A., Burgess, R.J., Vue, T.Y., Johnson, J.E., and Morrison, S.J. (2014). Prospective identification of functionally

Cell

distinct stem cells and neurosphere-initiating cells in adult mouse forebrain. eLife 3, e02669.

Mira, H., Andreu, Z., Suh, H., Lie, D.C., Jessberger, S., Consiglio, A., San Emeterio, J., Hortigüela, R., Marqués-Torrejón, M.Á., Nakashima, K., et al. (2010). Signaling through BMPR-IA regulates quiescence and long-term activity of neural stem cells in the adult hippocampus. Cell Stem Cell 7, 78–89.

Müller, U., Steinhoff, U., Reis, L.F., Hemmi, S., Pavlovic, J., Zinkernagel, R.M., and Aguet, M. (1994). Functional role of type I and type II interferons in antiviral defense. Science 264, 1918–1921.

Obernier, K., Cebrian-Silla, A., Thomson, M., Parraguez, J.I., Anderson, R., Guinto, C., Rodas Rodriguez, J., Garcia-Verdugo, J.M., and Alvarez-Buylla, A. (2018). Adult neurogenesis is sustained by symmetric self-renewal and differentiation. Cell Stem Cell 22, 221–234.

Oh, J., Lee, Y.D., and Wagers, A.J. (2014). Stem cell aging: mechanisms, regulators and therapeutic opportunities. Nat. Med. 20, 870–880.

Ortega, F., Gascón, S., Masserdotti, G., Deshpande, A., Simon, C., Fischer, J., Dimou, L., Chichung Lie, D., Schroeder, T., and Berninger, B. (2013). Oligodendrogliogenic and neurogenic adult subependymal zone neural stem cells constitute distinct lineages and exhibit differential responsiveness to Wnt signalling. Nat. Cell Biol. 15, 602–613.

Ottone, C., Krusche, B., Whitby, A., Clements, M., Quadrato, G., Pitulescu, M.E., Adams, R.H., and Parrinello, S. (2014). Direct cell-cell contact with the vascular niche maintains quiescent neural stem cells. Nat. Cell Biol. 16, 1045–1056.

Picelli, S., Faridani, O.R., Björklund, A.K., Winberg, G., Sagasser, S., and Sandberg, R. (2014). Full-length RNA-seq from single cells using Smart-seq2. Nat. Protoc. 9, 171–181.

Ponti, G., Obernier, K., Guinto, C., Jose, L., Bonfanti, L., and Alvarez-Buylla, A. (2013). Cell cycle and lineage progression of neural progenitors in the ventricular-subventricular zones of adult mice. Proc. Natl. Acad. Sci. USA 110, E1045–E1054.

Qiu, X., Mao, Q., Tang, Y., Wang, L., Chawla, R., Pliner, H.A., and Trapnell, C. (2017). Reversed graph embedding resolves complex single-cell trajectories. Nat. Methods 14, 979–982.

Ravichandran, S., and Del Sol, A. (2017). Identifying niche-mediated regulatory factors of stem cell phenotypic state: a systems biology approach. FEBS Lett. 591, 560–569.

Rezza, A., Sennett, R., and Rendl, M. (2014). Adult stem cell niches: cellular and molecular components. Curr. Top. Dev. Biol. 107, 333–372.

Rieger, M.A., Hoppe, P.S., Smejkal, B.M., Eitelhuber, A.C., and Schroeder, T. (2009). Hematopoietic cytokines can instruct lineage choice. Science 325, 217–218.

Robinson, M.D., and Oshlack, A. (2010). A scaling normalization method for differential expression analysis of RNA-seq data. Genome Biol. 11, R25.

Seib, D.R.M., Corsini, N.S., Ellwanger, K., Plaas, C., Mateos, A., Pitzer, C., Niehrs, C., Celikel, T., and Martin-Villalba, A. (2013). Loss of Dickkopf-1 restores neurogenesis in old age and counteracts cognitive decline. Cell Stem Cell 12, 204–214.

Shalek, A.K., Satija, R., Adiconis, X., Gertner, R.S., Gaublomme, J.T., Raychowdhury, R., Schwartz, S., Yosef, N., Malboeuf, C., Lu, D., et al. (2013). Single-cell transcriptomics reveals bimodality in expression and splicing in immune cells. Nature 498, 236–240.

Shalek, A.K., Satija, R., Shuga, J., Trombetta, J.J., Gennert, D., Lu, D., Chen, P., Gertner, R.S., Gaublomme, J.T., Yosef, N., et al. (2014). Single-cell RNA-seq reveals dynamic paracrine control of cellular variation. Nature 510, 363–369.

Shi, Z., Geng, Y., Liu, J., Zhang, H., Zhou, L., Lin, Q., Yu, J., Zhang, K., Liu, J., Gao, X., et al. (2018). Single-cell transcriptomics reveals gene signatures and alterations associated with aging in distinct neural stem/progenitor cell subpopulations. Protein Cell 9, 351–364.

Shook, B.A., Manz, D.H., Peters, J.J., Kang, S., and Conover, J.C. (2012). Spatiotemporal changes to the subventricular zone stem cell pool through aging. J. Neurosci. 32, 6947–6956.

Silva-Vargas, V., Maldonado-Soto, A.R., Mizrak, D., Codega, P., and Doetsch, F. (2016). Age-dependent niche signals from the choroid plexus regulate adult neural stem cells. Cell Stem Cell 19, 643–652.

Solano Fonseca, R., Mahesula, S., Apple, D., Raghunathan, R., Dugan, A., Cardona, A., O'Connor, J., and Kokovay, E. (2016). Neurogenic niche microglia undergo positional remodeling and progressive activation contributing to age-associated reductions in neurogenesis. Stem Cells Dev. 25, 542–555.

Stewart, W.J. (1994). An Introduction to the Numerical Solution of Markov Chains (New Jersey: Princeton University Press).

Stiehl, T., and Marciniak-Czochra, A. (2011). Characterization of stem cells using mathematical models of multistage cell lineages. Math. Comput. Model. 53, 1505–1517.

Villeda, S.A., Luo, J., Mosher, K.I., Zou, B., Britschgi, M., Bieri, G., Stan, T.M., Fainberg, N., Ding, Z., Eggel, A., et al. (2011). The ageing systemic milieu negatively regulates neurogenesis and cognitive function. Nature 477, 90–94.

Walter, D., Lier, A., Geiselhart, A., Thalheimer, F.B., Huntscha, S., Sobotta, M.C., Moehrle, B., Brocks, D., Bayindir, I., Kaschutnig, P., et al. (2015). Exit from dormancy provokes DNA-damage-induced attrition in haematopoietic stem cells. Nature 520, 549–552.

Yu, G., Wang, L.-G., Han, Y., and He, Q.-Y. (2012). clusterProfiler: an R package for comparing biological themes among gene clusters. OMICS 16, 284–287.

Zhu, Y., Demidov, O.N., Goh, A.M., Virshup, D.M., Lane, D.P., and Bulavin, D.V. (2014). Phosphatase WIP1 regulates adult neurogenesis and WNT signaling during aging. J. Clin. Invest. 124, 3263–3273.

Ziebell, F., Martin-Villalba, A., and Marciniak-Czochra, A. (2014). Mathematical modelling of adult hippocampal neurogenesis: effects of altered stem cell dynamics on cell counts and bromodeoxyuridine-labelled cells. J. R. Soc. Interface 11, 20140144.

Ziebell, F., Dehler, S., Martin-Villalba, A., and Marciniak-Czochra, A. (2018). Revealing age-related changes of adult hippocampal neurogenesis using mathematical models. Development 145, dev153544.

Cell

STAR★METHODS

KEY RESOURCES TABLE

REAGENT or RESOURCE	SOURCE	IDENTIFIER
Antibodies		
Anti-GLAST-PE (ACSA-1)	Miltenyi Biotec	Cat# 130-098-804; RRID:AB_10829184
Anti-CD45-APC-Cy7	BD	Cat# 557659; RRID:AB_396774
Anti-O4-APC (O4)	Miltenyi Biotec	Cat# 130-099-211; RRID: AB_2659794
Anti-CD133 (Prominin I) PerCP-eFluor710	eBioscience	Cat# 46-1331-80; RRID:AB_10671147
Alexa Fluor 488 EGF complex	Life Technologies	Cat# E-13345; RRID: N/A
Anti-PSA-NCAM-PE-Vio770 (2-2B)	Miltenyi Biotec	Custom-made
Anti-Doublecortin (DCX)	Millipore	Cat# AB2253; RRID:AB_1586992
Anti-GFAP (GA5)	Millipore	Cat# MAB3402; RRID:AB_94844
Anti-GFAP	Millipore	Cat# AB5804; RRID:AB_10062746
Anti-GFP	Aves Labs	Cat# GFP-1020; RRID:AB_10000240
Anti-Sox2	R&D Systems	Cat# AF2018, RRID:AB_355110)
Anti-Sox2 (Y-17)	Santa Cruz	Cat# sc-17320; RRID:AB_2286684
CD31-PE	Thermo Fisher Scientific	Cat# 12-0311-81, RRID:AB_465631)
CD11b-APC	BD Biosciences	Cat# 553312, RRID:AB_398535
Ter119 APC-Cy7	BioLegend	Cat# 116223, RRID:AB_2137788
Prominin1-APC	Thermo Fisher Scientific	Cat# 17-1331-81, RRID:AB_823120
anti-BrdU	Abcam	Cat# ab6326, RRID:AB_305426
anti-S100b	Abcam	Cat# ab52642, RRID:AB_882426
anti-GFAP	Thermo Fisher Scientific	Cat# 13-0300, RRID:AB_2532994
anti-Ki67	Novus	Cat# NB 600-1252, RRID:AB_578001
anti-IL33	R and D Systems	Cat# AF3626, RRID:AB_884269
anti-beta III-tubulin	Sigma-Aldrich	Cat# T8578, RRID:AB_1841228
anti-GFAP	Sigma-Aldrich	Cat# G3893, RRID:AB_477010
anti-NG2	Millipore	Cat# AB5320, RRID:AB_11213678
Mouse IgG2B Isotype control	R&D Systems	Cat# MAB0041, RRID:AB_357347
anti-sFRP5	Novus	Cat# MAB6266
Armenian Hamster IgG Isotype control	Biolegend	Cat# 400902
Armenian Hamster anti-CXCL10	Custom made	Urs Christen
Chemicals, Peptides, and Recombinant Proteins		
Triton X-100	Sigma-Aldrich	Cat# T9284
dNTP mix	Fermentas	Cat# R0192
First-strand buffer	Invitrogen	Cat# 18064-014
DTT	Invitrogen	Cat# 18064-014
Superscript II reverse transcriptase	Invitrogen	Cat# 18064-014
Recombinant RNase inhibitor	Clontech	Cat# 2313A
Betaine	Sigma-Aldrich	Cat# 61962
Magnesium chloride	Sigma-Aldrich	Cat# M8266
KAPA HiFi HotStart ReadyMix	KAPA Biosystems	Cat# KK2601
Agencourt Ampure XP beads	Beckman Coulter	Cat# A 63881
BrdU	Sigma-Aldrich	Cat# B5002
TMZ	Sigma-Aldrich	Cat# T2577-25mg
TAM	Sigma-Aldrich	Cat# T5648-5G

Continued

REAGENT or RESOURCE	SOURCE	IDENTIFIER
human EGF	Promokine	Cat# C-60170
human FGF	ReliaTech	Cat# 300-003
Interferon β	Millipore	Cat# IF011
Interferon α	Millipore	Cat# IF009
Recombinant Mouse sFRP-5 Protein, CF	R&D	Cat# 7195-SF-050
Recombinant Wnt3a protein	Peprotech	Cat# 315-20
Critical Commercial Assays		
Neural Tissue Dissociation Kit (T)	Miltenyi Biotec	Cat# 130-093-231
X-tremeGene 9 transfection reagent	Roche	Cat# 6365779001
Nextera XT Sample Preparation Kit	Illumina	Cat# FC-131-1096
Neural Tissue Dissociation Kit (P)	Miltenyi Biotec	130-092-628
Dual-Luciferase Reporter Assay System	Promega	Cat# E1910
Picopure RNA Isolation Kit	Thermo Fisher Scientific	Cat# KIT0214
SMARTer Ultra Low RNA Illumina (10 rxns)	Takara	Cat# 634935
NEBNext Ultra DNA Library Prep Kit for Illumina - 24 rxns	New England Biolabs	Cat# E7370S
Spike ins	Ambion	Cat# 4456739
Chromium SingleCell 3′ Library and Gel Bead Kit v2,4rxns	10x Genomics	Cat# 120267
Deposited Data		
Bulk population, Smartseq2 and Chromium 3′ sc RNaseq	This Paper	GEO: GSE115626
Full Code for Data Analysis	This Paper	http://martin-villalba-lab.github.io/ (released once accepted)
Experimental Models: Organisms/Strains		
Mouse: Tlx-CreER^{T2}	Liu et al., 2008	Haikun Liu (kind gift)
Mouse: B6.129-Gt(ROSA)26Sortm1(EYFP)Cos/J	The Jackson Laboratory	JAX: 006148
C57BL/6	Janvier	JAX:000664
IFNRKO (IFNAR−/−IFNGR−/−)	Huang et al., 1993; Müller et al., 1994	N/A
Tlx-CreERT2-eYFP	Liu et al., 2008	N/A
TCF/Lef:H2B-GFP	Ferrer-Vaquer et al., 2010	MGI:4881498
Recombinant DNA		
Renilla	N/A	(Berger et al., 2017)
pCS2+	N/A	(Berger et al., 2017)
Topflash	N/A	(Berger et al., 2017)
Sequence-Based Reagents		
TSO: (5′AAGCAGTGGTATCAACGCAGAGT ACATrGrG+G-3′)	N/A	(Picelli et al., 2014)
ISPCR oligo: (5′-AAGCAGTGGTATCAA CGCAGAGT-3′)	N/A	(Picelli et al., 2014)
Oligo dT: (5′-AAGCAGTGGTATCAACGC AGAGTACT30VN-3′)	N/A	(Picelli et al., 2014)
Software and Algorithms		
Fiji ImageJ	Open source: https://imagej.nih.gov/ij/	Version 2.0.0-rc-15/1.49i, RRID:SCR_002285
Adobe Illustrator CS5.1	Adobe Systems	Version 15.1.0, RRID:SCR_010279
Prism 6	GraphPad	Version 6.0b, RRID:SCR_002798

(Continued on next page)

Cell

Continued

REAGENT or RESOURCE	SOURCE	IDENTIFIER
Cell Ranger	10X Genomics	Version 2.0.0, https://software.10xgenomics.com/single-cell-gene-expression/software/downloads/
FastQC	N/A	Version 0.11.4, https://www.bioinformatics.babraham.ac.uk/projects/fastqc/, RRID:SCR_014583
Btrim	N/A	Version 0.3.0, http://graphics.med.yale.edu/trim/, RRID:SCR_011836
Samtools	N/A	Version 1.3, http://samtools.sourceforge.net/, RRID:SCR_002105
RSEM	N/A	Version 1.2.18, https://github.com/deweylab/RSEM, RRID:SCR_013027
STAR	Dobin et al., 2013	Version 2.4.0g, https://github.com/alexdobin/STAR/releases, RRID:SCR_015899
Picard Toolkit	Broad Institute	Version 1.123, https://broadinstitute.github.io/picard, RRID:SCR_006525
Trinity	Haas et al., 2013	Version 2.2.0, https://github.com/trinityrnaseq/trinityrnaseq/
HTSeq	N/A	Version 0.6.1p2, https://htseq.readthedocs.io/en/release_0.10.0/, RRID:SCR_005514
Integrative Genomics Viewer (IGV)		https://www.broadinstitute.org/igv, RRID:SCR_011793
R		Version 3.4.4, http://www.r-project.org, RRID:SCR_001905
Seurat	N/A	Version 2.2.0, https://satijalab.org/seurat/, RRID:SCR_016341
monocle	N/A	Version 2.4.0, https://bioconductor.org/packages/release/bioc/html/monocle.html, RRID:SCR_016339
clusterProfiler	Yu et al., 2012	Version 3.4.4, https://bioconductor.org/packages/release/bioc/html/clusterProfiler.html
DESeq2	N/A	Version 1.16.1, https://bioconductor.org/packages/release/bioc/html/DESeq2.html, RRID:SCR_015687
biomaRt	N/A	Version 2.32.1,https://bioconductor.org/packages/release/bioc/html/biomaRt.html
pheatmap	N/A	Version 1.0.8, https://github.com/raivokolde/pheatmap, RRID:SCR_016418
Other		
Gentle MACS Dissociator	Miltenyi Biotec	Cat# 130-093-235
Alzet Model 1007D	Charles River	Cat# 0000290
Alzet Brain Infusion Kit 3	Charles River	Cat# 0008851
gentleMACS C Tubes	Miltenyi Biotec	Cat# 130-093-237
Lab-Tek Chamber Slides (8 wells)	Thermo Fisher Scientific	Cat# 177402

CONTACT FOR REAGENT AND RESOURCE SHARING

Further information and requests for resources and reagents should be should be directed to and will be fulfilled by the Lead Contact, Ana Martin-Villalba (a.martin-villalba@dkfz-heidelberg.de).

EXPERIMENTAL MODEL AND SUBJECT DETAILS

Mouse strains

Male C57BL/6 mice were purchased from Janvier or bred in house at the DKFZ Center for Preclinical Research facility. Male IFNRKO (Huang et al., 1993; Müller et al., 1994) (IFNAR−/−IFNGR−/−) 2 and 22 MO were backcrossed to a C57BL6 background. Male and female Tlx-CreER^{T2}YFP (Liu et al., 2008) were used according to the protocols in Figure S5. Male 2 MO and 8 MO TCF/Lef:H2B/GFP

were used to assess TCF/Lef activity (Ferrer-Vaquer et al., 2010). Animals had *ad libitum* access to food and water and were kept under a 12hr light-12hr dark cycle. All procedures were approved by the Regierungpräsidium Karlsruhe.

METHOD DETAILS

Implantation of mini-osmotic pumps
Mice were anaesthetized with isofluorane and a mini-osmotic pump (Alzet Model 1007D, Brain infusion Kit 3) with a volume of 100 μL and a flow rate of 0.5 μl/hour containing different antibodies was implanted 1.1 mm lateral and 0.5 mm posterior to the bregma according to the manufacturer's instructions.

BrdU
BrdU (Sigma) was dissolved in 0.9% saline solution at 10 mg/ml and was heated at 50°C until it was completely dissolved. For intraperitoneal injections (I.P) appropriate amount of BrdU was administered to match the concentrations indicated at Figure S5. For BrdU administration in drinking water, BrdU was dissolved in water with 0.1% sucrose in a concentration of 1 mg/ml. For embryonic labeling timed-pregnant TLX-CreER^{T2}YFP mothers were injected with two shots of BrdU (50 mg/kg) six hours apart at embryonic day 14 (E14).

Temozolomide (TMZ) treatment
Temozolomide dissolved in 75% saline 25%DMSO (or 0.9% saline in control animals) was injected daily I.P. in a concentration of 100mg/kg. BrdU was administered I.P. at 100mg/kg and mice were sacrificed 2 hours after injection or as indicated in the protocol.

Tamoxifen
TLX-CreER^{T2}YFP pups embryonically labeled with BrdU, were given two shots of Tamoxifen (Sigma-Aldrich, 83.35 mg/kg, 9 Sunflower seed oil:1 100% EtOH) 12 hours apart from postnatal day 28 till 32. TLX-CreER^{T2}YFP mice 2, 7 and 22 MO were given two shots of Tamoxifen (50mg/kg) 12 hours apart for 5 days.

Treatments with neutralizing antibodies
Mini-osmotic pumps were filled with 100 μL of neutralizing antibodies or isotype controls at the following concentrations: for sFRP5 neutralization 333 μg/ml of Mouse IgG2B Isotype control (Novus, MAB0041) or anti-sFRP (Novus, MAB6266) dissolved in PBS were used. For CXCL10 neutralization 500 μg/ml Purified Armenian Hamster IgG Isotype control (Biolegend, 400902) or Armenian Hamster anti-CXCL10 from Urs Christen were used.

FACS analysis and sorting
Generation of single cell suspension and stainings for FACS analysis or FACS sorting were performed as described in Llorens-Bobadilla et al. (2015). Briefly, mice were sacrificed, SVZ was microdissected and single cell suspension was obtained using the Neural Tissue Dissociation kit with Trypsin (or Papain when staining for CD31+ and CD11b+ cells) and Gentle MACS dissociator (Miltenyi). For staining the following antibodies were used: Ter119 APC-Cy7 (Biolegend, 1:100), O4 APC and APC-Cy7 (Miltenyi, 1:50), CD45 APC-Cy7 (BD, 1:200), GLAST (ACSA-1)-PE and APC (Miltenyi, 1:20), Prominin1-APC and PerCP-eFluor 710 (eBioscience, 1:75), Alexa488::EGF (Life Technologies, 1:100), PSA-NCAM PE-Cy7 Miltenyi, 1:75), CD31-PE (BD, 1:100), CD11b-APC (BD, 1:100) and Sytox Blue (Life Technologies, 1:1000).

Time-lapse video microscopy
Sorted quiescent and active NSCs from 2 and 22 MO mice were plated and tracked. *Ex vivo* activation of quiescent NSCs was rare. Hence our analysis was restricted to aNSCs. Video microscopy of primary adult neural stem cell cultures was performed with a Cell Observer (Zeiss) at constant conditions of 37°C and 8% CO$_2$ as previously described (Ortega et al., 2013). Phase contrast images were acquired every 5 minutes for 5-6 days using a 20 X phase contrast objective (Zeiss) and an AxioCamHRm camera with a self-written VBA module remote controlling Zeiss AxioVision 4.7 software (Rieger et al., 2009). Time-lapse videos were assembled by using ImageJ whereas single-cell tracking was carried out using a self-written computer program (TTT) (Hilsenbeck et al., 2016).

Immunostainings
Mice were transcardially perfused with ice cold HBSS and 4% PFA. Brains were post-fixed in 4% PFA O/N and subsequently immersed in 30% sucrose. 15 μm sections were prepared using a cryotome. For stainings of E-LRCs and TCF/Lef reporter mice, 50 μm sections were prepared at the vibratome. Sections were blocked for unspecific labeling in 0.25% Triton X-100, 3% horse serum for 1 hr at RT and consequently with primary antibody mix at 4°C O/N. Sections were washed and incubated with secondary antibodies in blocking buffer for 90' at RT. Primary antibodies used were: anti-DCX (guinea-pig, Merck Millipore, 1:1000), anti-GFP (chicken, Aves, 1:1000), anti-Sox2 (goat, Santa Cruz, 1:500), anti-BrdU (rat, abcam, 1:100), anti-S100b (rabbit, abcam, 1:100), anti-GFAP (rat, thermo fischer, 1:1000), anti-Ki67 (rabbit, novus, 1:200), anti-IL33 (goat, novus, 1:150). 4-8 sections, 6 sections apart were used for immunostainings.

Cell

Cells

Labtek chambers were coated with PDL/laminin and NSCs were seeded at a density 20000/cm^2 and treatments followed. Cells were blocked for unspecific staining in 0.25% Triton X-100, 3% horse serum for 30' at RT and consequently with primary antibody mixture containing combination of anti-beta III-tubulin (mouse IgG2b, Sigma, 1:300), anti-GFAP (mouse IgG1, Sigma, 1:800), anti-NG2 (rabbit, Millipore, 1:500) or anti-Sox2 (goat, Santa Cruz, 1:500), anti-Ki67 (rabbit, novus, 1:200) at 4°C O/N.

Isolation and cultivation of NSCs *in vitro*

SVZ was microdissected and single cell suspension was prepared using the Neural Tissue Dissociation kit with Papain (Miltenyi). Cells were transferred in Neurobasal A (NBM A) medium containing 2% B27 supplement serum (GIBCO), 1% L-Glutamine, 2 μg/ml of Heparin, 20 ng/μl of human FGF basic growth factor (ReliaTech), 20 ng/μl of human EGF (Promokine). Cells were not used for longer than 10 passages. For treatment with recombinant mouse interferons α/β, 160 U/ml (Millipore) were added in NSC medium and cells were incubated for 48 h.

Luciferase Reporter (Topflash) assays

Luciferase reporter assays were performed as previously described (Berger et al., 2017). Briefly, HEK293T cells were grown in 96-well plates and transfected with 5 ng Topflash, 1 ng Renilla and 44 ng empty vector (pCS2+) DNA using X-tremeGene 9 transfection reagent (Roche) and following the supplier's protocol. 24 h after transfection, cells were stimulated with the indicated conditions: CHAPS control or recombinant Wnt3a protein (Peprotec, 180 ng/mL) with or without recombinant sFRP5 protein (Novus, 5 μg/mL). To examine if neutralizing sFRP5 antibody can inhibit recombinant sFRP5, recombinant Wnt3a together with sFRP5 and the neutralizing antibody (Novus, 5 or 25 μg/mL) were pre-incubated at room temperature for 30 minutes before applied to the cells. After 24 h, cells were harvested and Luciferase activity was determined following the manufacturer's manual (Promega, Dual-Luciferase Reporter Assay System). Values are presented as Firefly activity normalized to Renilla values.

Sphere assay

aNSCs (CD45-O4-Ter119-GLAST+CD133+EGFR+) (Figure S6A) from 2, 7 and 22 MO were sorted in 96 wells containing 3x growth factors and the diameter of spheres was measured 5 days later using a LEICA table microscope.

Comet assay

qNSCs (CD45-O4-Ter119-GLAST+CD133+EGFR-) and aNSCs (CD45-O4-Ter119-GLAST+CD133+EGFR+) (Figure S6A) were isolated in NBM A with B27 and comet assay was performed as described in Walter et al. (2015) with the difference that low-melting-temperature agarose was purchased from Biozym.

Microscopy

Confocal images were acquired with a LEICA SP5 microscope with a 405 nm laser, an argon multiline (458-514 nm), a helium neon 561nm and a helium neon 633nm laser. For quantification of stainings of vibratome sections we acquired tilescans from the whole ventricle and z stacks of 20 μm with 1 μm apart in a resolution of 2048x2048. For quantification of cryosections we acquired tilescans of the whole ventricle combined with z stacks covering the tissue thickness in a resolution of 1024x1024. Finally, for imaging of stained cells from *in vitro* cultures 6-12 fields of view were obtained at a resolution of 512x512. For all images 40- or 63x oil immersed objectives were used. Quantifications were performed with Fiji and the plug-in cell counter navigating through the stacks. For quantification of TCF/Lef activity in different domains, we measured the total length of the SVZ occupied by cells and assigned the upper 1/3 as dorsal and the lower 2/3 as lateroventral. Highly autofluorescent speckles called lipofuscin were observed in the aging brain. Speckles present in all fluorescent channels were visually excluded during quantifications.

Analysis of Smart-seq2 single-cell RNA-seq data
Sorting for Smart-seq2

Preparation was performed as described in Llorens-Bobadilla et al. (2015). Briefly, we sorted for CD45-O4-CD133+GLAST+ NSCs (Figure S6A). Single NSCs were handpicked and libraries according to Smart-seq2 were prepared. 4 mice of 23 MO were pulled per replicate.

In total, we performed RNA-seq on 145 old single cells in parallel with published data from Llorens-Bobadilla et al. (2015) which were used as young counterparts. All the steps for cell sorting and library preparation were identical. Through quality control steps, we removed 12 cells and kept 133 cells for downstream analysis. For isolation of astrocytes, we sorted for GLAST+O4-CD45- from cortex or striatum, cells were handpicked and libraries were prepared according to Smart-seq2 as previously described in Llorens-Bobadilla et al. (2015).

Quality control steps are described as following.

Smart-seq2 library preparation

Single cell RNA-seq libraries were prepared according to the Smart-seq2 protocol as described by Picelli et al. (2014). Single cells were pipetted in lysis buffer and were frozen O/N. Subsequently, cells were thawed and reverse transcription was performed with an

oligo(dT) primer and a locked nucleic acid-containing template-switching oligonucleotide. ERCC Spike-Ins (Ambion) were added to 8 randomly selected samples at a dilution 1/1000000. Full-length cDNA was amplified with the KAPA HiFi polymerase by 20 cycles of PCR. Samples with high quality of cDNA were further processed after assessment on a High Sensitivity Bioanalyzer chip (Agilent). Libraries for Illumina sequencing were generated with the Nextera XT Sample preparation protocol after extending the tagmentation to 8 minutes and doing a double bead clean up with 0.8X AMPure XP SPRI beads after PCR amplification of 9 cycles.

Read trimming and mapping
Raw read quality was checked by FASTQC (http://www.bioinformatics.babraham.ac.uk/projects/fastqc/). Trimming of adaptor sequences in raw reads was performed before alignment with Btrim64 (http://graphics.med.yale.edu/trim) (Kong, 2011). Mapping of trimmed reads to the mouse genome (ENSEMBL Release 78/GRCm38.p3) was done using STAR 2.4.0g (Dobin et al., 2013). Mapping results to the genome were visually inspected with the Integrative Genome Viewer (https://www.broadinstitute.org/igv/).

RNA-seq data quality metrics
RNA-seq data quality metrics of each cell, including total reads, transcriptome mapped reads and transcriptome mapped rate was calculated by picard-tools-1.123 (https://broadinstitute.github.io/picard/) (Table S4).

Gene Expression Matrices
Gene expression matrices were generated as previously described (Shalek et al., 2013, 2014). Gene expression levels as transcripts per million (TPM) and fragments per kilobase of transcript per million mapped reads (FPKM) were produced with RSEM 1.2.18 with default parameters. Additionaly, we used Trinity (Haas et al., 2013) (https://github.com/trinityrnaseq) based on edgeR (Robinson and Oshlack, 2010) to perform TMM (trimmed mean of M-values) an additional normalization on FPKM (abbreviated TMM-FPKM), to be able to compare samples with differences in the total cellular RNA production.

Quality control of single-cell RNA-seq data
The qualities of single cell RNA-seq libraries were checked by the combination alignment rates and number of genes detected with TPM > 1. Cells showing substantially fewer numbers of genes detected (TPM > 1) and/or lower mapping rates (two times standard deviation) than others were filtered out. We also filtered out cells in which Gapdh and Actb are lowly expressed (TPM < 100) and Slc1a3-negative NSCs (TPM < 10). In total, 132 single cells passed quality control and were used in downstream analysis.

ERCC spike-in controls
The quality of single-cell RNA-seq data was assessed by adding known amount of 92 ERCC spike-in RNA transcripts in 8 random cells and the expression levels of these transcripts in TPM correlated well to the known amount.

Monocle pseudotime assignment
The TPM values data from young and old cells were loaded together into the monocle2 R package using its relative2abs function (Qiu et al., 2017). During the creation of the CellDataSet object lowerDetectionLimit was set to 0.5 and a negbinomial expression family was selected. The ordering genes used for the pseudotime calculation were selected based on a mean_expression > = 0.5 and dispersion_empirical > = 3 * dispersion_fit. Pseudotime assignments for all cells were saved into a file for later use.

Expression of DNA damage associated genes
To check for the expression of DNA damage associated genes in the data, a heatmap was created using the pheatmap R package (version 1.0.8) from a list of manually selected genes. The TPM values for those genes were log2 transformed before plotting

PCA
PCA was run on the TPM values of the 2000 most variable genes in the dataset and for all cells PC1 and PC2 were plotted against each other in a scatterplot. PCA plots were also prepared for individual subpopulations and cells colored by age of the animal.

DE analysis Smart-seq2
Differentially expressed genes between astrocytes and qNSC1 were determined using a likelihood ratio test as described in Llorens-Bobadilla et al. (2015). The log-transformed TPM gene expression values of the up and downregulated genes (> 2 fold-change, adjusted p value < 0.1) from qNSC1, qNSC2 and astrocytes in the Smart-seq2 data were plotted as a heatmap (using pheatmap R package).

Differentially expressed genes of each activation state against all others were determined by t test as provided by Seurat. Differentially expressed genes between cells from old and young mice within each activation state were determined by DESeq2 after exclusion of non-expressed genes. In addition, we calculated differentially expressed genes between cells from old versus young mice within each activation state by the difference of the mean log-transformed TPM expression values divided by the mean SD and ranked by the nominal p value (t test).

Cell

Euclidean distance calculation
The euclidean distances between neighboring activation states along the neurogenic lineage (qNSC1, qNSC2, aNSC1, aNSC2) between cells from 2 MO and 23 MO mice within the same subpopulations were calculated on the first 5 principal components and their distribution was plotted using density estimation (ggplot2 R package).

Bulk RNA sequencing
Bulk RNA seq
For Bulk sequencing we sorted 1000 events of different populations based on the following marker combinations: Endothelial CD45-CD31+, Microglia CD45+CD11b+, NSCs CD45-CD133+GLAST+, Neuroblasts CD45-GLAST-PSA-NCAM+ (Figure S6C). Since the CD31 epitope was sensitive to trypsin we did the endothelial and microglia cell isolation with the Neural Tissue Dissociation kit (papain). Briefly, RNA was isolated with arcturos pico pure kit and cDNA was prepared using the SMARTer Ultra Low Input RNA for Illumina Sequencing – HV. Finally, libraries were prepared for sequencing using the NEBNext Ultra DNA Library Prep Kit for Illumina. 2 2 MO and 4 19 MO mice were pulled per replicate.
Processing RNA-seq data of bulk
We prepared biological duplicates of libraries from young and old populations from NSCs, endothelial, microglial and neuroblast cell types. Quality control of cell population RNA-seq data was performed as the single-cell RNA-seq data. After quality control raw reads were mapped to the mouse reference genome GRCm38 (ENSEMBL release 78/ GRCm38.p3) using STAR_2.4.0g1. Genes annotated in ENSEMBL release 78 were quantified with HTSeq 0.6.1p2. Differential expression analysis was performed with DESeq2.

GO term enrichment analysis
The lists of differentially expressed genes from comparing old to young for NSCs, neuroblasts, microglia, endothelial cells were filtered for those genes with an adjusted p value of less than 0.05 and then supplied to the clusterCompare and simplify functions of the clusterProfiler R package (Yu et al., 2012) to prepare a dotplot of the top 8 GO categories from each celltype using the "biological process" ontology.

Expression of Innate immune response genes
Significantly upregulated genes in the comparisons of 19MO to 2MO samples for each cell type were checked for annotation in the InnateDB and Ensembl gene IDs were obtained using the biomaRt R package (version 2.32.1). The annotated genes were highlighted on MA plots of the comparisons for the respective celltypes. In the 7MO to 2MO NSC MA plot the genes from the 19MO versus 2MO comparison were highlighted.

10x Chromium 3′ sequencing
Sorting for 10x Chromium 3′
Single cell suspension was prepared as described before. To ensure that there is enough starting material for the Chromium 3′ 10x platform, we sorted CD45-O4-Ter119-GLAST+ (Figure S6B). 8000 FACS events underwent the downstream process according to the manufacturer's details. 4 2MO and 8 22 MO mice were pulled for each library.
Library preparation, sequencing and mapping
We prepared one library from cells isolated from old and another with cells isolated from young mice (both with 10x Genomics Chemistry: Single Cell 3′ v2) and sequenced them on a HiSeq 4K PE 100. The Cell Ranger Software (Ver. 2.0.0) provided by 10x Genomics was used to map the reads (provided as fastq files) to the mouse reference genome (ENSEMBL Release 78/GRCm38.p3) for each sample individually and the two samples were merged according to the Cell Ranger manual.

Analysis with the Seurat package
The Seurat R package (version 2.2.0) was used for further inspection and data analysis. First all genes, which showed expression in less than 3 cells were discarded. Then the cells were filtered for further analysis based on the following parameters: expression of at least 1500 genes and at most 4500 genes (to exclude cell duplets), less than 10% of transcripts coming from mitochondrial genes. After these filters 3066 cells remained (out of 3937 cells initially provided by the CellRanger pipeline) (Table S4). The transcript counts were log transformed, the number of detected genes, number of detected unique molecular barcodes (UMIs) and the percentage of mitochondrial gene expression was regressed out and transformation to z-scores was performed, by subtraction of the mean and division by the standard deviation. As we compared cycling and non-cycling cells we aimed to reduce the influence of the cell cycle states on cells from the same cell type, while keeping the cell cycle signal, which is an important component of NSC activation. As described in the Seurat package documentation, all cells were scored for the cell cycle states G1-, G2/M- and S-phase and then the difference between the G2/M- and S-phase scores was regressed out to discard the cell cycle states difference, while keeping the cell cycle signal. Genes were determined to be variable based on the following parameters: mean expression between 0.0125 and 4 and log variance to mean ratio of at least 0.5. Those variable genes were used as input for PCA. This dimensionally reduced data was used for clustering using Seurat's graph-based clustering approach with a resolution parameter of 0.8, selecting the first 8 principal components as input. 18 cells were excluded from the further analysis as they also showed expression of the leukocytic marker gene PTPRC (CD45) or ependymal marker genes (Jacquet et al., 2009) and thus are possibly contaminations of cells from these celltypes.

For visualization t-SNE was run on the first 8 principal components. To check whether clusters were separating based on the age of the animals and if there are batch effects, PCA and t-SNE plots were generated for all cells and individual subpopulations and cells were colored according to the animal age (Figure 4C). Gene expression of individual marker genes in the determined clusters was checked by coloring the cells in the t-SNE plot according to gene expression strength. The identity of the subpopulations was determined by manual inspection of the gene expression values for previously used marker genes and comparison of differentially expressed genes of each cluster (compared to all the other clusters in the dataset). Those were compared to differentially expressed genes from the Smart-seq2 single-cell RNA sequencing data (Llorens-Bobadilla et al., 2015). The aNSC0 subpopulation is composed of two clusters which showed a difference in the expression of immediate early response genes, while the aNSC1 subpopulation contains two clusters showing a seperation based on the predicted cell cycle phase. A phylogenetic tree based on average cells for all determined identities was constructed based on the first 8 PCs using the BuildClusterTree function. The average gene expression for all genes was calculated between young and old cells in NSCs, cell types along the neurogenic lineage as well as OPCs and ODs and plotted in a scatterplot with log10 transformed axes.

Monocle pseudotime assignment

Raw transcript counts from the CellRanger output were also loaded into the monocle2 R package (version 2.4.0) and filtered to exclude cells identified as OD or OPCs. A cellDataSet object was prepared as described for the Smart-seq2 sequencing data. The ordering genes were selected to have a mean expression $>= 0.6$ and an empirical dispersion $>= 3 *$ dispersion fit. Pseudotime computation results were saved and used together with the cluster identities from the Seurat clustering to check if the identified clusters agree with the predicted pseudotime by plotting the identity-colored cells according to their monocle predicted reduced dimensions dimensions and vice versa coloring cells in the tSNE plot by their predicted pseudotime value.

DE and GO term enrichment analysis

To find differentially expressed genes between cell from 2 and 22 MO mice the DESeq2 R package (version 1.16.1) was used. The clusterProfiler R package (version 3.4.4) was used for GO term enrichment analysis with its clusterCompare and simplify functions using the "biological process" ontology. Genes with an adjusted p value < 0.05 and an absolute Fold Change > 2 were used. Differentially expressed genes of each activation state against all others were determined by t test as provided by Seurat. DE genes between cells from old and young mice within each activation state were determined by DESeq2 as provided by Seurat. In addition, we calculated differentially expressed genes between young versus old cells within each activation state by the difference of the mean log-transformed expression values divided by the mean SD and ranked by the nominal p value (t test).

Euclidean distance calculation

The euclidean distances between neighboring activation states along the neurogenic lineage (qNSC1, qNSC2, aNSC0, aNSC1, aNSC2, TAP, NB) as well as between qNSC1 and OD or between cells from 2MO and 22MO mice within the same subpopulations were calculated on the first 8 principal components and their distribution was plotted using density estimation (ggplot2 R package).

QUANTIFICATION AND STATISTICAL ANALYSIS

Statistics were performed as indicated in each figure. All multiple comparisons were performed with GraphPad Prism's one-way Anova function, which also performs a Tukey-Kramer test, reporting p values adjusted to control family-wise error rate for the family comprising comparisons of each group against all other groups.

DATA AND SOFTWARE AVAILABILITY

RNaseq raw sequence data is available from GEO (accession number: GSE115626). All the analysis is described in the Method Details. The complete R/Bioconductor software package will available upon acceptance on the authors' webpage (https://martin-villalba-lab.github.io/).
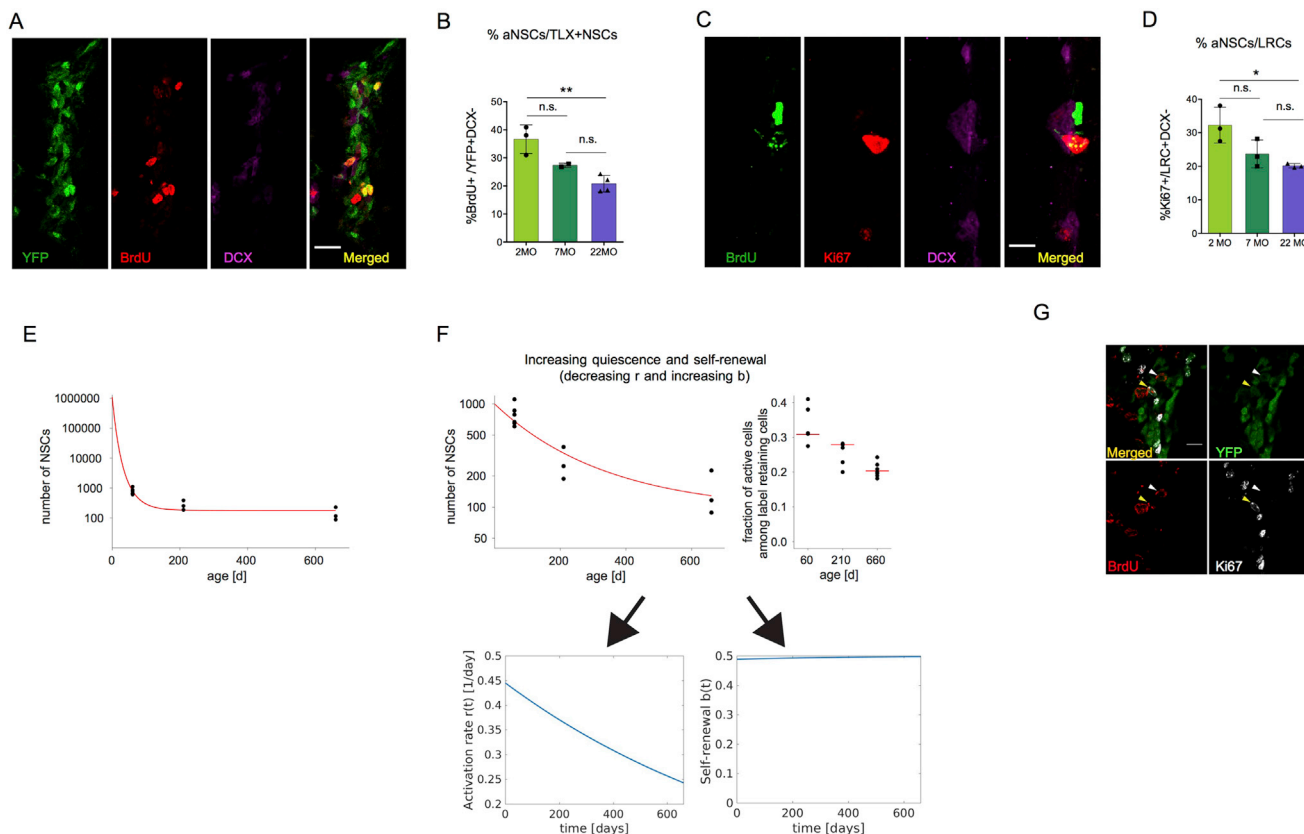
Figure S1. Quiescence of NSCs Increases upon Aging, Related to Figure 1

A) Representative picture of cells from the V-SVZ 2MO TLX-CreER^{T2}YFP (scale bar: 20 μm). B) Fraction of BrdU+ cells among YFP+DCX- cells in 2, 7 and 22 MO (Each data point represents one mouse; bar and whiskers denote mean ± SD; Tukey-Kramer multiple-comparisons test). C) Representative picture of a Ki67+LRC+ cell in the SVZ of 22 MO. (Scale bar:10 μm) D) Fraction of Ki67+ cells among LRC+DCX- in 2, 7 and 22MO (n = 3 mice/group; bar and whiskers denote mean ± SD; Tukey-Kramer multiple-comparisons test). E) Fit of the neurogenesis model with increase of self-renewal during aging. The cell counts at age 0 are in the order of 10^6. F) Upper panel: Fit of the neurogenesis model with simultaneous increase of quiescence and self-renewal during aging. Lower panels: Model with simultaneous increase of quiescence and self-renewal during aging: Time course of self-renewal fraction and activation rate. The activation rate from quiescence significantly decreases in time. The self-renewal fraction only slightly changes at younger ages. The red curves correspond to model simulations. Each black dot denotes experimental data of one mouse. G) Representative pictures of embryonically BrdU-labeled YFP+ cells that are Ki67+ (yellow arrow) or Ki67- (white arrow) (scale bar: 10 μm). *p < 0.05; **p < 0.01; ***p < 0.001; n.s.: not significant.
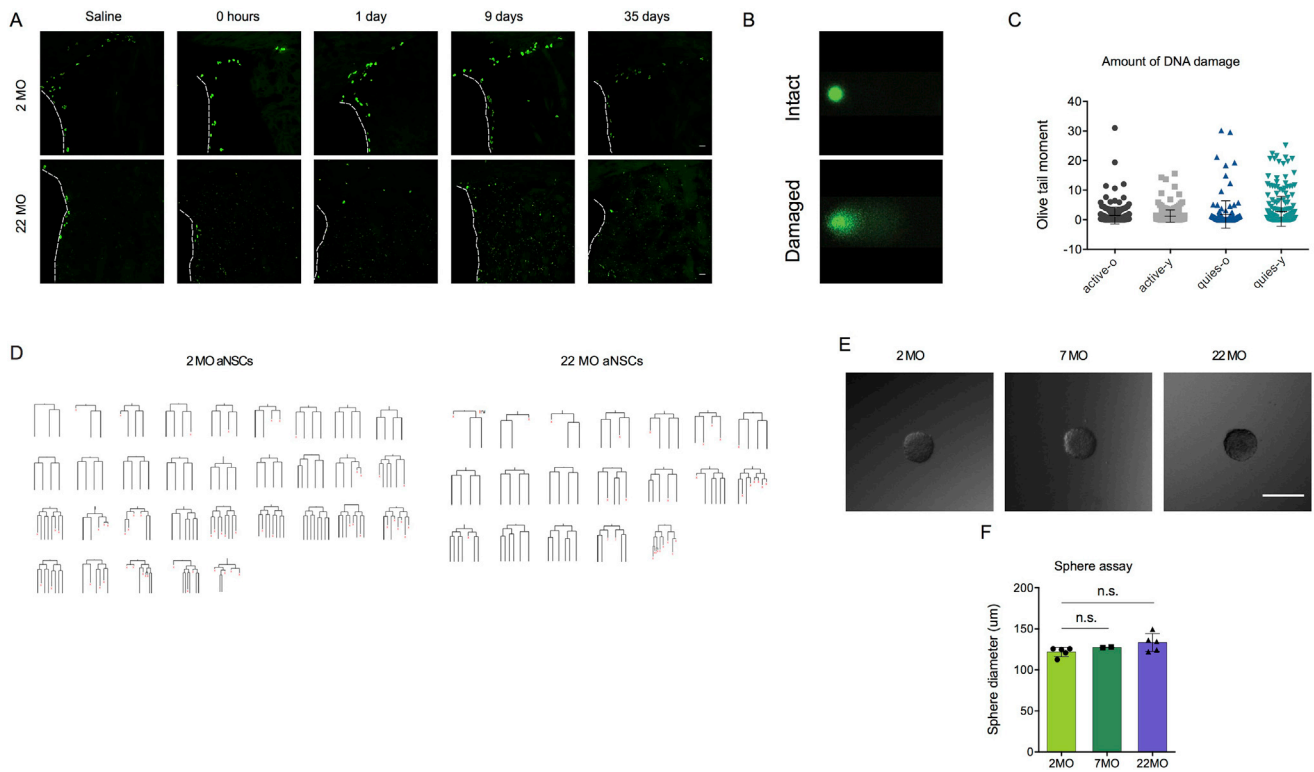
Figure S2. DNA Damage Does Not Increase upon Aging and Old aNSCs Have Similar Properties to Young, Related to Figure 2

A) Maximum intensity projection micrographs (scale bar: 10 μm) of dorsal SVZ from 2 and 22 MO mice at different time points after TMZ injection. (note the increase in autofluorescent lipofuscin speckles all over the 22 MO brains). B) Representative pictures of intact or damaged nuclei after 5Gy gamma irradiation. C) Quantification of the olive tail moment (active old n = 257 cells, active young n = 274 cells, quiescent old n = 150 cells, quiescent young n = 245 cells). D) Lineage trees of 2 MO and 22 MO aNSCs. E) Representative pictures of spheres derived from single aNSCs from 2, 7 and 22 MO mice (scale bar: 200 μm). F) Quantification of sphere diameter (2 MO and 22 MO n = 4, 7MO n = 2; bar and whiskers denote mean ± SD; Tukey-Kramer multiple-comparisons test). n.s.: not significant.
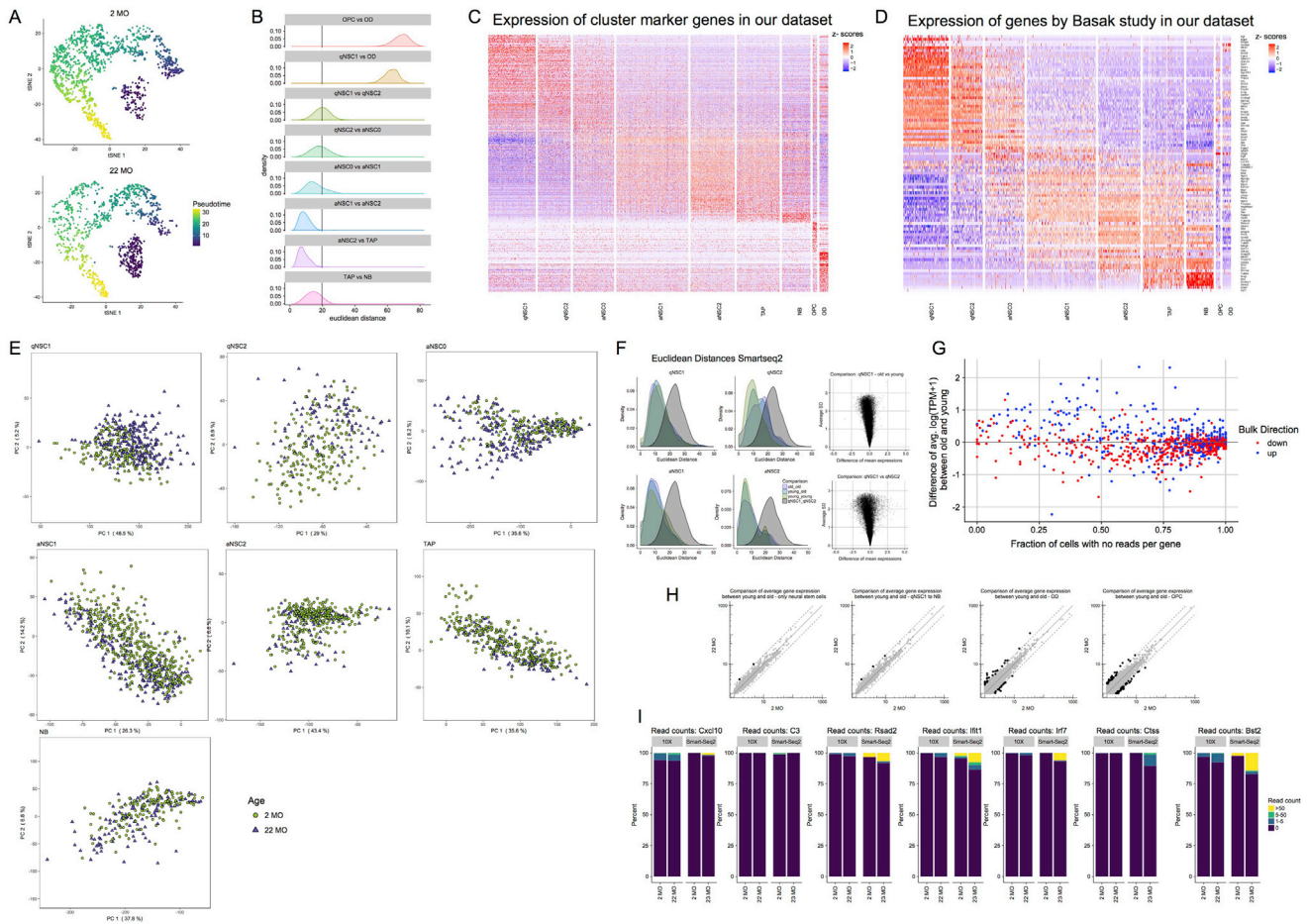
Figure S3. Transcriptomic Analysis, Related to Figures 3 and 4

A) tSNE map of cells from the neurogenic lineage colored by pseudotime as assigned by monocle2 (10x 3′ Chromium). B) Distributions of euclidean distances between cells from different activation states. Although there is a gap between the qNSC1 and qNSC2 in the t-SNE plot the comparison of the distance distributions shows that the distance between qNSC1 and qNSC2 is similar to the distance of qNSC2 and aNSC0, which are not separated by a gap. The distance distribution of qNSC1 compared to OD as expected shows a higher distance between these cell types, while the aNSC clusters are closer together (10x 3′ Chromium). C) Heatmap of differentially expressed genes for the identified cell clusters (gene-wise z-scores). Columns (cells) are sorted by their monocle assigned pseudotime from left to right (for cells from the neurogenic lineage), while cells from OPC and OD are added to the right without further sorting. Rows (genes) were ordered by increasing onset of expression along the pseudotime from top to bottom. Differentially expressed genes for OPC and OD were added to the bottom. See Table S1 (10x 3′ Chromium). D) Heatmap displaying expression of selected genes (gene-wise z-scores) from recently published sc RNAseq data of young SVZ (Basak et al., 2018) in cells of our study sequenced with the 10x genomics platform (10x 3′ Chromium). E) PCA plots of individual subpopulations of NSCs sequenced (10x 3′ Chromium). F) Comparison of euclidean distance distributions between cells of the same activation state from young and old, young and young, old and old mice. Euclidean distance between qNSC1 and qNSC2 serves as reference. (Smart-seq2). The right panel shows a detailed view of changes in mean expression and SD for each gene between old and young within qNSC1 (upper) and in the transition qNSC1→qNSC2 in young and old (lower). G) Scatterplot of genes in the Smart-seq2 data that were differentially expressed upon aging in bulk NSCs. y axis indicates the difference of the average log-transformed TPM values between old and young. x axis denotes the fraction of cells without any reads for this gene in either old or young. To this end we calculated the fraction separately for young and old and used the larger value. Color denotes the direction of change in the bulk sequencing data. H) Scatterplots comparing gene expression between 22 and 2 MO mice, averaged over all NSCs, the neurogenic lineage, ODs or OPCs. Dotted lines represent 2 fold-change (genes > 2 FC are shown in black) (10x 3′ Chromium). I) Barplots representing the percentage of cells with read counts stratified in 4 different intervals (0, 1-5, 5-50, > 50) of top genes related to immune response upregulated in Bulk sequencing between old and young NSCs in (10x 3′ Chromium and Smart-seq2).
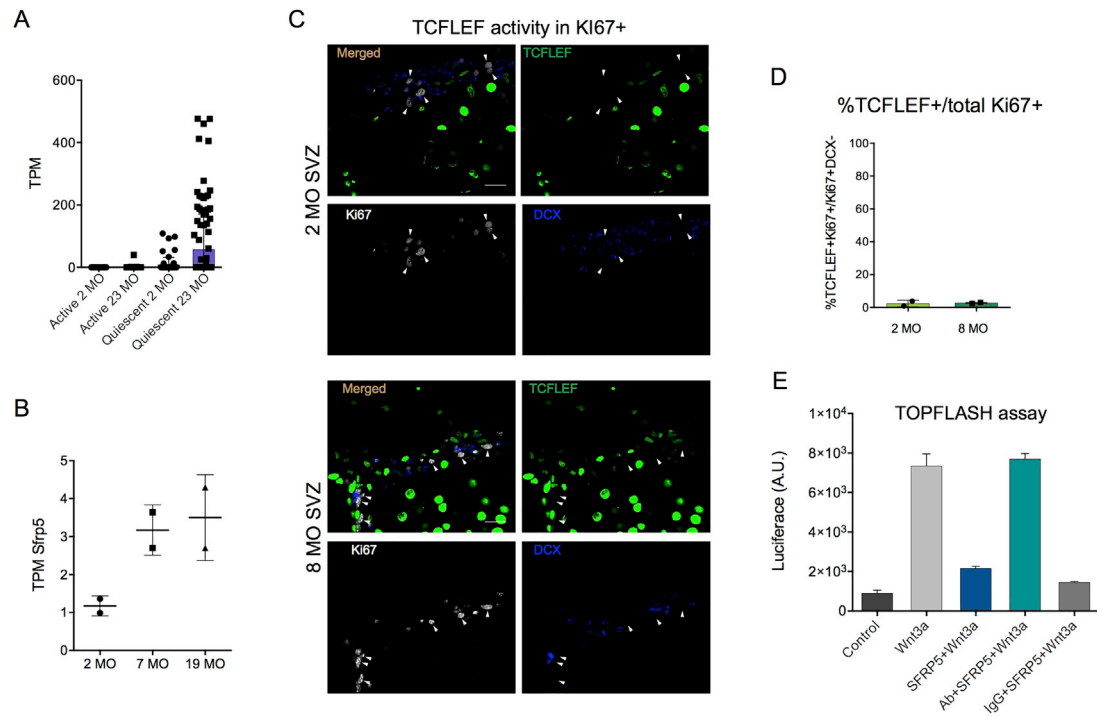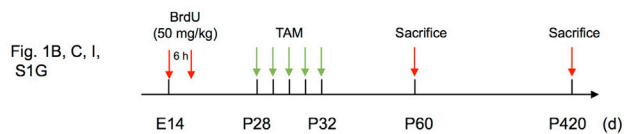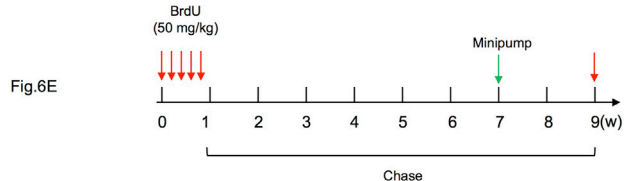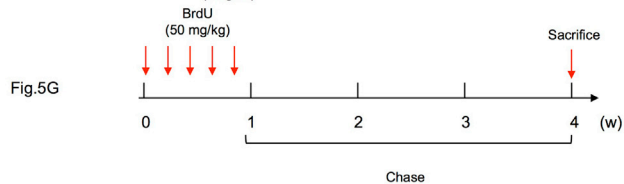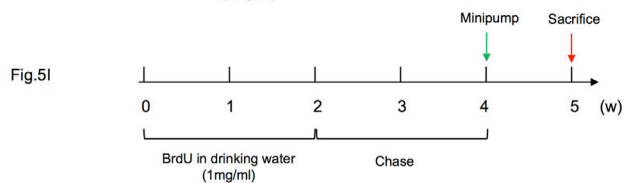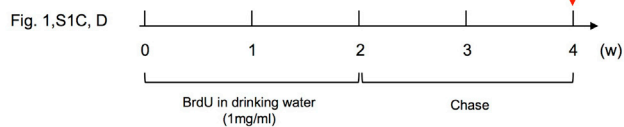
Figure S4. Related to Figure 6

A) Expression of Sfrp5 from Smart-seq2 single cell data (bar and whiskers denote mean ± SD). B) Expression of Sfrp5 in bulk populations of NSCs at 2, 7 and 19 MO NSCs (dots represent biological replicates). C) Representative pictures of TCF/Lef expression among Ki67+ cells (scale bars: 20 μm) in 2 and 8 MO mice (arrows indicate examples of Ki67+ cells that are TCF/Lef-). D) Quantification of TCF/LEF+ among Ki67+ cells (2 MO n = 2, 8MO n = 3; data shown as mean ± SD). E) TOPFLASH assay with HEK293 cells (Data shown as mean ± SD).
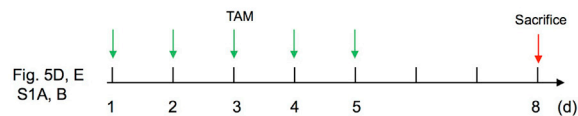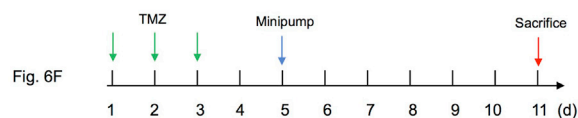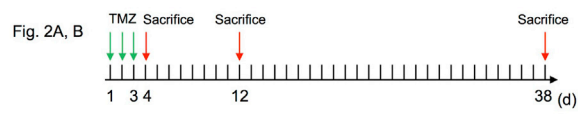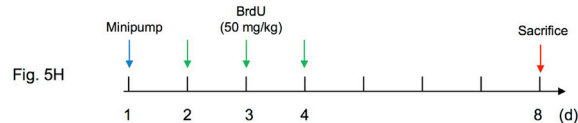
Figure S5. Related to Figures 1, 2, 5, 6, and S1

Experimental outlines of experiments across the article. A) Approaches to label and follow e-LRC or LRC NSCs. B) Labeling of proliferating cells in the SVZ with a 2 hr pulse of BrdU. C) Labeling of newly-born NBs arriving at the olfactory bulb.
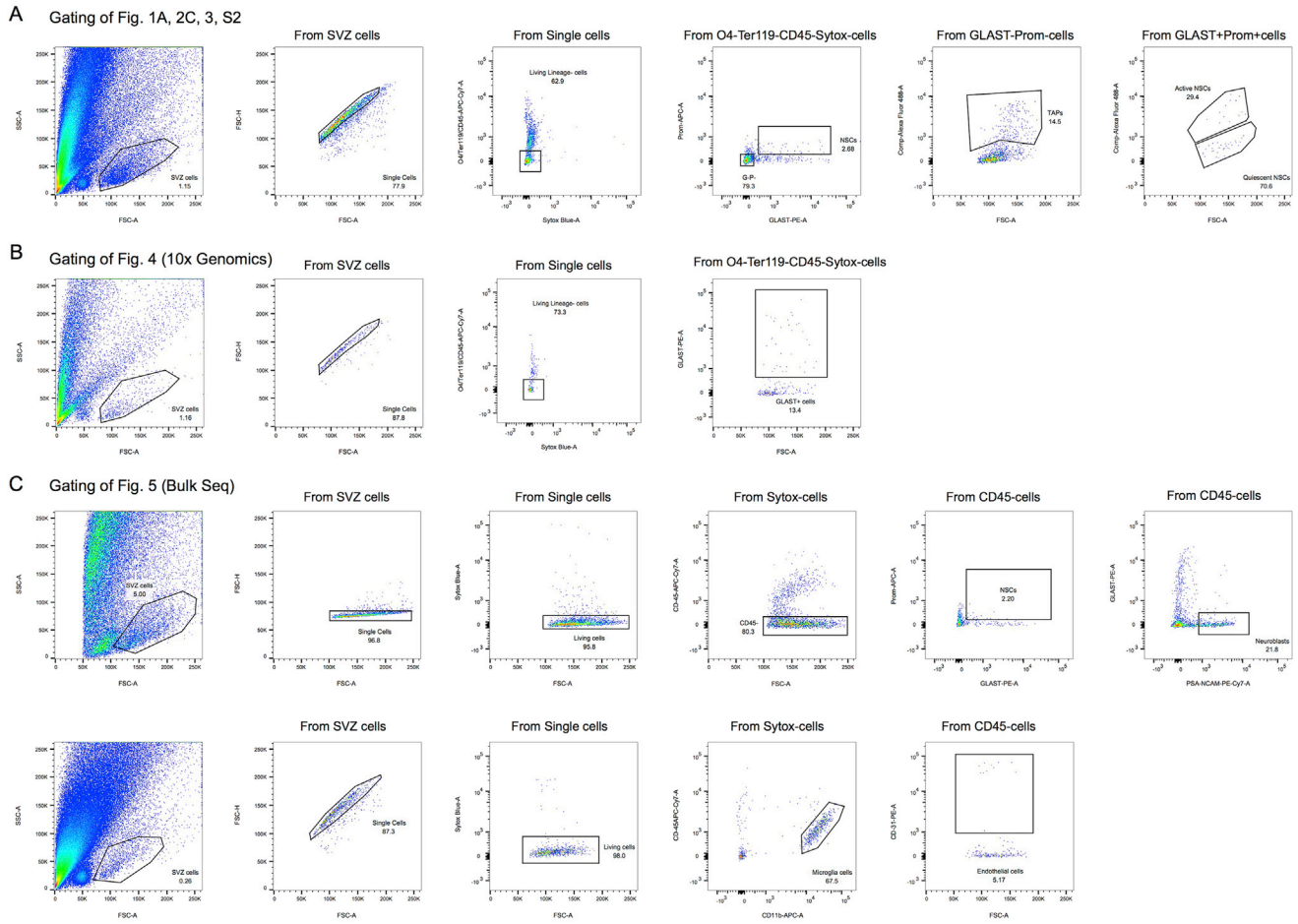
Figure S6. Related to Figures 1, 2, 3, 4, 5, and S2

FACS strategies followed for the isolation and analysis of V-SVZ cell populations. A) Strategy for the isolation of qNSCs, aNSCs and TAPs. B) Strategy for preparation of libraries for 10x Chromium 3′. C) Strategy followed to isolate different populations of cells from the V-SVZ niche.